Pergamon

PII S0016-7037(01)00854-7

Efremovka 101.1: A CAI with ultrarefractory REE patterns and enormous enrichments of Sc, Zr, and Y in Fassaite and Perovskite

A. El Goresy,[1,2,*] E. Zinner,[3] S. Matsunami,[4] H. Palme,[5] B. Spettel,[1] Y. Lin,[6] and M. Nazarov[7]

[1]Max-Planck-Institut für Chemie, 50674 Mainz, Germany
[2]Max-Planck-Institut für Kernphysik, Saupfercheckweg 1, 69117 Heidelberg, Germany
[3]McDonnell Center for the Space Sciences and Physics Department, Washington University, St. Louis, MO 63130-4899, USA
[4]Department of Earth Sciences, Miyagi University of Education, Aramaki Aoba, Sendai 980, Japan
[5]Institut für Mineralogie und Geochemie der Universität, 50674 Köln, Germany
[6]Guangzhou Institute of Geochemistry, Chinese Academy of Sciences, Guangzhou 510640, China
[7]Vernadsky Institute of Geochemistry and Analytical Chemistry, Moscow, Russian Federation

Abstract—Inclusion 101.1 from the CV3 carbonaceous chondrite Efremovka is a compact Type A Ca-Al-rich inclusion (CAI) highly enriched in ultrarefractory (UR) oxides. It is the first complete CAI with a UR rare earth element (REE) pattern found in a CV3 chondrite. The inclusion is petrographically complex and was formed in a multistage process. It consists of several lithologically unrelated units.

The core contains abundant Y- and Zr-perovskite, Sc- and Zr-rich fassaite, and metallic FeNi enclosed in melilite. All mineral species (except spinel) in all lithological units exhibit the same basic UR REE pattern. Four different populations of perovskites are distinguished by different Y/Zr ratios. A few of the perovskites have Y/Zr ratios similar to those obtained from crystal/liquid fractionation experiments. Perovskites from the other three populations have either chondritic, lower than chondritic Y/Zr ratios or extremely low Zr contents. Ca isotopic ratios differ among three perovskites from different populations, demonstrating a variety of sources and formational processes. Most fassaites crystallized in situ through reaction between the CAI liquid and preexisting perovskites. This process induced redistribution of Zr, Y, Sc, and V between perovskite and fassaite, thus overprinting the original abundances in perovskite. Fassaite reaction rims around FeNi metals are also encountered. They are enriched in V, which was gained from the metal through oxidation of V in metal during fassaite crystallization. The relative abundances of Zr, Y, and Sc in perovskites are complementary to the abundances of these elements in Sc- and Zr-fassaite, indicating subsolidus partitioning of these elements between the two phases. Perovskites are enriched in Y and depleted in Sc and Zr in comparison to fassaites.

The core contains two complete captured CAIs, several sinuous fragments, and fine-grained polygonal refractory fragments. An assemblage of andradite-wollastonite-hedenbergite and pure metallic iron is encountered as enclaves in the interior of some sinuous fragments. Metallic Fe and wollastonite formed by reduction of preexisting andradite and hedenbergite nebular alteration products upon inclusion in the highly reduced CAI melt. Numerous spinel clusters and framboids with varying V_2O_3 and Cr_2O_3 concentrations are enclosed in individual melilite crystals in the host CAI and captured CAIs. The rim sequence of the host consists of six layers (from the inside outward): (a) FeO-poor spinel, (b) Sc-bearing fassaite, (c) Al-diopside, (d) Al- and Ca-bearing olivine, (e) pure diopside, and (f) Ca-poor olivine. Like the constituents of the CAI core, all mineral layers of the rim sequence, except spinel, have the same UR REE pattern. However, the total REE abundances decrease systematically by 1 order of magnitude from layer 2 to layer 6. This feature strongly suggests formation of the rim sequence by successive condensation from a unique reservoir enriched in UR elements and excludes formation by flash heating. Petrography, mineral chemistry, REE, refractory lithophile element abundances, and Ca isotopic compositions demonstrate the complex multistage formation history of a CAI that on the surface looks like a regular Type A inclusion. *Copyright © 2002 Elsevier Science Ltd*

1. INTRODUCTION

Many Ca-Al-rich inclusions (CAIs) in carbonaceous chondrites display fractionated Group II rare earth element (REE) patterns with high enrichments in the light REEs (LREEs), low abundances of the some of the heavy REEs (HREEs), a negative Eu anomaly, positive Tm (and in some cases Yb) anomalies, and very low Lu abundances (Martin and Mason, 1974; Mason and Martin, 1977; Palme et al., 1982). Solid-liquid or solid-solid equilibration processes cannot produce this type of REE pattern. The origin of Group II patterns in refractory inclusions was explained to have resulted from fractional condensation leading to incorporation of the ultrarefractory (UR) elements Gd, Tb, Dy, Ho, Er, and Lu in perovskite, or hibonite (Boynton, 1975; Davis and Grossman, 1979, MacPherson and Davis, 1993).

Samples with REE patterns enriched in the UR elements, complementary to the Group II patterns, are very rare. Few such objects have been described in the literature (Boynton et al., 1980; Palme et al., 1982; Davis, 1984, 1991; Hinton et al., 1988; Ireland, 1990; Weber et al., 1995; Simon et al., 1996).

So far, no evidence has been found that any of the UR inclusions formed by evaporation of less refractory material. The lack of extensive isotopic mass-dependent fractionation of Ti in Ornans, Mighei, and Acfer 182 refractory inclusions

---

* Author to whom correspondence should be addressed (goresy @mpch-mainz.mpg.de).

Table 1. Chemical composition of Efremovka Ca-Al-rich inclusion (CAI) 101 consisting of 101.1 and 101.2 and of Efremovka bulk determined by instrumental neutron activation analysis.

%	Efremovka 101	SD	Efremovka bulk	SD		Efremovka 101	SD	Efremovka bulk	SD
Mg	9.85	5	13.77	5	Mo	3.84	20	1.4	20
Al	13.59	3	1.46	3	Ru	3.6	18	1.4	10
Ca	9.17	5	1.53	5	Sb	0.025		0.074	10
Ti	0.35	5	0.10	5	La	4.04	3	0.513	5
Fe	10.52	3	19.25	3	Ce	10.7	6	0.970	20
					Nd	7.8	13	0.315	15
ppm					Sm	2.64	3	0.319	5
Na	1310	3	1430	3	Eu	0.409	3	0.112	5
Cl	70	14	204		Tb	0.45	32	0.076	25
K	120	5	134	10	Dy	3.04	7	0.450	30
Sc	86.6	3	10.3	3	Ho	0.73	13	0.120	10
V	276	3	82.0	5	Yb	1.1	4	0.295	10
Cr	2800	3	3590	3	Lu	0.37	9	0.037	20
Mn	570	3	1410	3	Hf	1.75	20	0.170	15
Co	257	3	593	3	Ta	0.29	11		
Ni	5950	4	13705	4	W	0.58	18	0.9	20
Zn	115	9	109	10	Re	0.17	9	0.065	5
Ga	3.64	10	6.33	10	Os	2.57	8	0.785	8
As	0.59	8	1.60	8	Ir	2.11	3	0.701	3
Se	3.56	30	8.37	6	Pt	4.0	25	1.61	10
Br	0.57	8	0.74	8	Au	0.060	5	0.151	3
Sr	74	15			Th	<0.35			
Zr	<70				U	<0.1			

CAI 101 + 102: 29.44 mg; Efremovka bulk: average two samples each ≈200 mg; SD = standard deviation in %.

(Davis, 1991; Weber et al., 1995) indicates that these samples formed by condensation. All UR CAIs lack not only isotopic mass fractionation expected to result from evaporation (Davis et al., 1990; Davis and Hashimoto, 1995; Floss et al., 1996) but
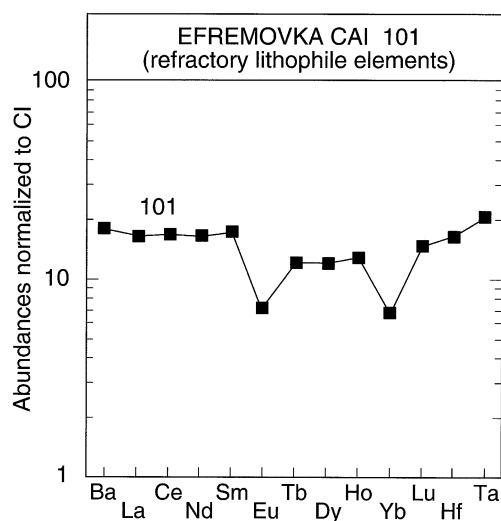

Fig. 1. Abundances of refractory lithophile elements in Ca-Al-rich inclusion (CAI) 101 analyzed by instrumental neutron activation analysis. Note that the analyzed sample includes 101.1 + 101.2 and some adhering Efremovka matrix. The bulk rare earth element (REE)–pattern is a Group III pattern with negative Yb and Eu anomalies, not uncommon in Allende CAIs. This pattern is a combination of a superrefractory pattern of 101.1, a Group II pattern of 101.2 and a flat REE pattern of the adhering matrix.
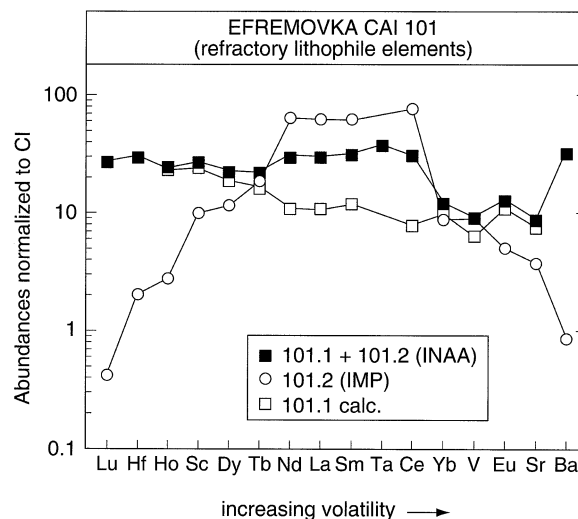

Fig. 2. Refractory lithophile element abundances in the total 101 sample, in 101.2 as determined by ion probe analysis and in 101.1 as calculated by mass balance. Elements are arranged according to volatility. The bulk pattern is more or less flat from Lu to Ce (see also Fig. 1), 101.2 has a Group II pattern, and the calculated pattern for 101.1 is superrefractory in accord with the patterns of individual phases of this Ca-Al-rich inclusion (CAI).

also any Ce depletions, which are consistently produced in laboratory evaporation experiments from a wide variety of starting materials, in particular from chondritic starting compositions (Ireland et al., 1992; Wang et al., 1993; Davis et al., 1995; Floss et al., 1996).

Table 2. Calculated trace element concentrations in Efremovka inclusion 101.2.

Element	Spot 1	Spot 2
K	36.6	37.7
Sc	57.2	47.9
V	472	393
Cr	15,181	13,348
Sr	29.9	32.3
Y	1.01	0.81
Zr	2.93	2.75
Nb	0.94	0.85
Ba	1.99	3.06
Hf	0.24	<0.19
La	14.6	12.9
Ce	45.3	35.7
Pr	6.07	5.22
Nd	28.5	24.5
Sm	9.23	7.96
Eu	0.28 ± 0.05	0.22 ± 0.04
Gd	4.30 ± 0.45	2.99 ± 0.40
Tb	0.64 ± 0.08	0.43 ± 0.07
Dy	2.86	2.41
Ho	0.15 ± 0.02	0.08 ± 0.02
Er	0.28 ± 0.03	0.20 ± 0.03
Tm	1.29	1.03
Yb	1.35	1.28
Lu	0.010 ± 0.010	0.015 ± 0.009

Concentrations are in ppm weight. 1σ errors due to countings statistics are given only if >10%.
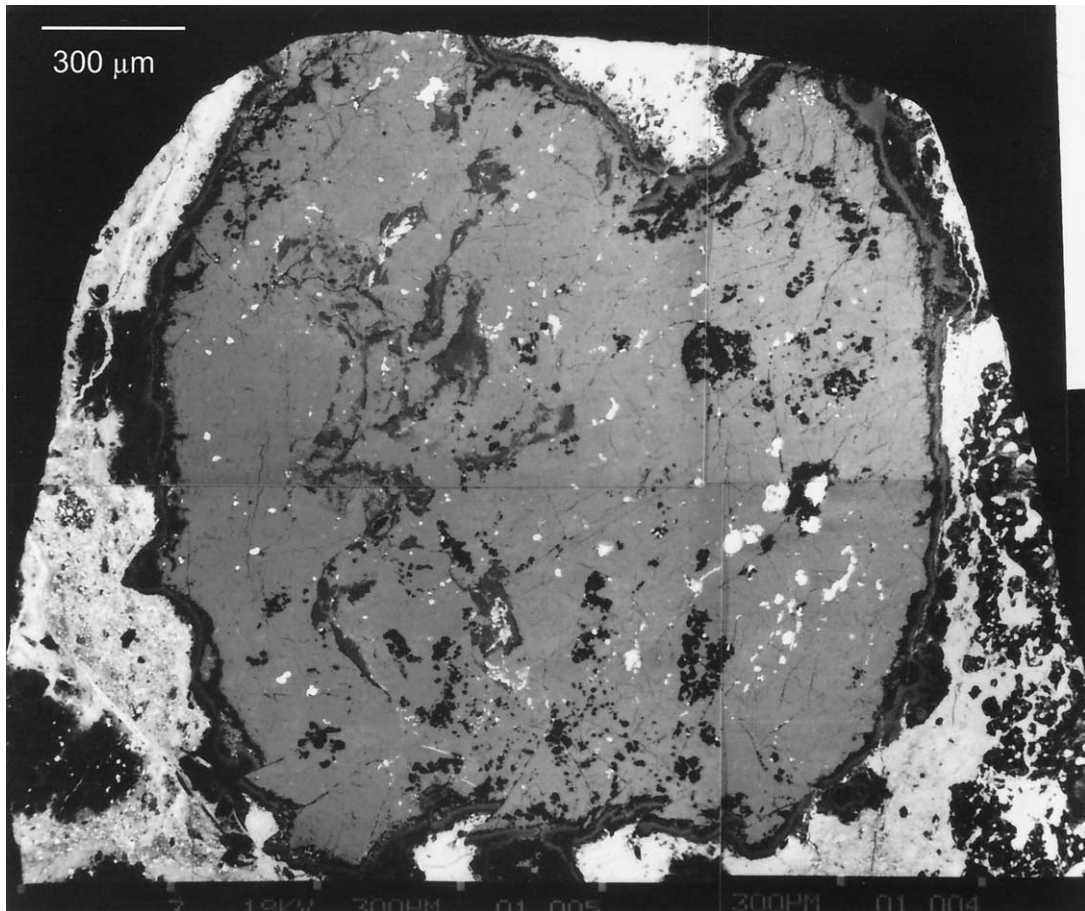
Fig. 3. A back scattered electron mosaic of Efremovka 101.1 Ca-Al-rich inclusion. Notice the high abundance of metal blebs and coarse perovskite grains in the right and of sinuous fragments in the left portion.

The puzzling behavior of perovskite and hibonite as carriers of UR patterns in some inclusions but as carriers of volatile REEs with excesses in the least refractory REEs in other inclusions has been noticed before (Kimura et al., 1993; Weber et al., 1995). Therefore, it has been suggested that the UR component is not condensing in perovskite (Kimura et al., 1993). Except for the fact that most UR patterns seem to be associated with perovskite and hibonite, the detailed mineral assemblages vary from one UR inclusion to another.

It has been noted previously that all UR inclusions have been reported from CO3 and CM2 chondrites, and none were found in CV3 chondrites, although Group II patterns are well represented among CAIs from other types of meteorites, especially from Allende. In this paper, we report the discovery of a complete UR inclusion from the Efremovka CV3 chondrite. Efremovka belongs to the reduced subgroup of CV3 chondrites (McSween, 1977) that show only minor effects of secondary alteration.

We have mechanically separated 12 CAIs from Efremovka (CV3) for major and trace element measurements by instrumental neutron activation analysis (INAA) and subsequent petrographic, trace element, and isotopic investigations. Among these 12 CAIs, 2 (101.1 and 101.2) were found in close contact with each other. Only these two CAIs were investi-

gated. Because of their close spatial proximity, they were analyzed together for bulk chemistry, and a single polished section was prepared to avoid their destruction during mechanical separation. Efremovka 101.1 is an unusual Type A CAI. It has abundant melilite in its core and is surrounded by a complete rim sequence. In contrast, inclusion 101.2 consists of pink Cr-spinel and Ti-Al-fassaite with textures indicative of a quenched partial melt. Detailed petrography and chemistry of 101.2 will be presented elsewhere. Efremovka 101.1 was selected for the present study because of its primitive nature, the lack of alteration and oxidation veins in the core melilite and in rim layers, the diversity and complexity of its mineral assemblages, and the presence of enclosed objects, apparently foreign xenoliths and refractory fragments. During ion probe analysis, it became evident that we had encountered a unique complete CAI with UR REE patterns and enormous enrichments of Sc, Zr, and Y in several mineral species. In this paper, we present petrological, trace element, and isotopic data of the various minerals of the different lithological units in the core and of individual mineral layers of the rim sequence. A preliminary report on the petrologic, trace element, and Al-Mg isotopic characteristics of this inclusion was presented by El Goresy et al. (1993).
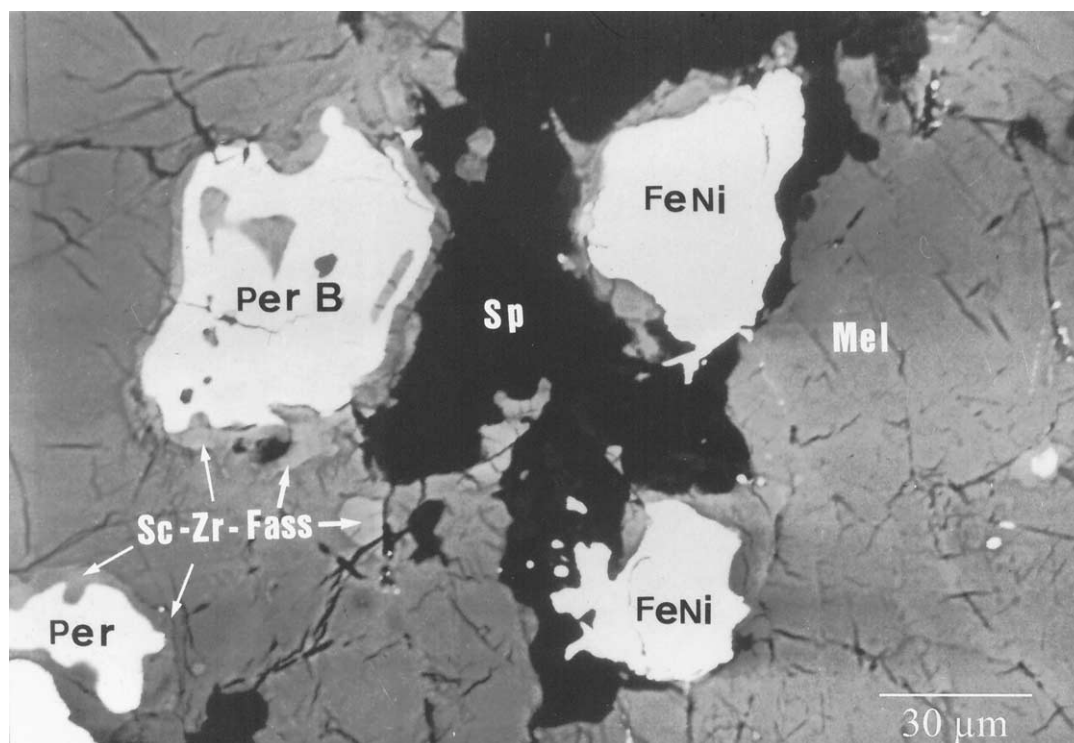
Fig. 4. A coarse-grained assemblage of FeNi-metal blebs, perovskite (Per), and spinel (Sp) in the right side of Figure 3. Metal and perovskite are surrounded by of Sc-Zr-fassaite rims (Sc-Zr-Fas). Notice that the Sc-Zr-fassaite rims separate the metal blebs and perovskite grains from the adjacent and the surrounding spinels.

2. ANALYTICAL METHODS

2.1. INAA

For the INAA, the sample containing 101.1, 101.2, and Efremovka matrix was irradiated in the TRIGA reactor of the Institut für Kernchemie (Universität Mainz) with a neutron flux of 7×10^{11} ncm^{-2}/sec^{-1} for 6 h. Analyses were done according to the procedure given in Wänke et al. (1977). After irradiation, γ-rays from the sample were counted in large Ge (Li) crystals. The resulting spectra were evaluated using the peak-fitting routine of Kruse (1979). Concentrations were calculated by irradiating and counting appropriate standards (for details, see Wänke et al., 1977) under identical conditions. The fragment containing the inclusions 101.1 and 101.2 was analyzed by INAA before preparation of the polished probe mount.

2.2. Reflected Light Microscopy, Scanning Electron Microscopy, and Electron Microprobe Analysis

The fragment containing 101.1 and 101.2 was vacuum impregnated in epoxy, and a composite polished section was prepared. Petrographic investigations were conducted in reflected light and both in the secondary electron and back scattered electron modes with a Cambridge 180S scanning electron microscope (SEM) at the Max-Planck-Institut für Kernphysik in Heidelberg, Germany. Semiquantitative analyses of the various mineral phases were made with the SEM using a Si (Li) energy dispersive spectrometer (resolution 147 eV at 5.898 keV). The chemical compositions of the coexisting phases were quantitatively determined with a computer-controlled, fully automated ARL-SEMQ electron microprobe using wavelength dispersive techniques at 15 kV accelerating voltage. The sample current was set at a value of 15 nA on the brass holder of the section. This allowed multiple checking of the electron beam drift within short intervals. Results of the electron microprobe analysis of the various mineral species are given in the section on mineral chemistry (section 3.3). Because of the small size (<5 μm) of some of the analyzed grains, a special analysis program

was employed that allows continuous checking of the electron beam position during an analytical run to ascertain that no spatial drift to a neighboring phase has occurred, as well as the readjustment of the beam spot to the desired position in case such a drift has taken place. An internal self-developed special X-ray deconvolution program was applied to correct for X-ray interferences such as Ca-K$_\beta$/Sc-K$_\alpha$, Sc-K$_\beta$/Ti-K$_\alpha$, Ti-K$_\beta$/V-K$_\alpha$, Y-L$_\beta$/Zr-L$_\alpha$, and Sc-L$_\alpha$ 2nd-order/Zr-L$_\alpha$. The 1σ standard deviations for the electron microprobe measurements are MgO: 0.05; Al$_2$O$_3$: 0.11; SiO$_2$: 0.02; CaO: 0.06; TiO$_2$: 0.02; FeO: 0.04; Sc$_2$O$_3$: 0.08; ZrO$_2$: 0.07; and Y$_2$O$_3$: 0.04. Åkermanite contents in melilites were determined for each analysis point by averaging the values obtained from the Mg, Al, and Si cations. All the reported melilite compositions calculated from the individual cations of these elements vary only slightly among individual analyses (2 to 3 mol.%). The beam current was continuously monitored during the analyses of each mineral species to secure that the measurements were carried out at very low beam drift rate. Long-duration measurements (100 s) were conducted on perovskites and melilites to obtain good counting statistics for the minor elements. As an additional precaution, pure synthetic stoichiometric perovskite and melilite standards were measured under the same conditions in 30-min intervals between the analyses sets of the Efremovka perovskites and melilites, respectively, to insure the accuracy of the elemental concentrations measured. The Ti^{3+} concentrations in perovskite and fassaite were calculated from the deviation of the number of total cations from the stoichiometric value (2 and 4, respectively) if all Ti was calculated as Ti^{4+} (see also Beckett, 1986). Errors in this mode of calculation for TiO$_2$ concentrations more than 4 wt.% can be ruled out because of the extremely low FeO contents in perovskite and fassaite. All analyses were corrected for drift, background, and matrix effects by using the procedures of Bence and Albee (1968) and Albee and Ray (1971) for oxides and silicates and conventional atomic number, absorption, and fluorescence corrections for metals and sulphides. Further details of the analytical procedures have been described previously (El Goresy et al., 1984).
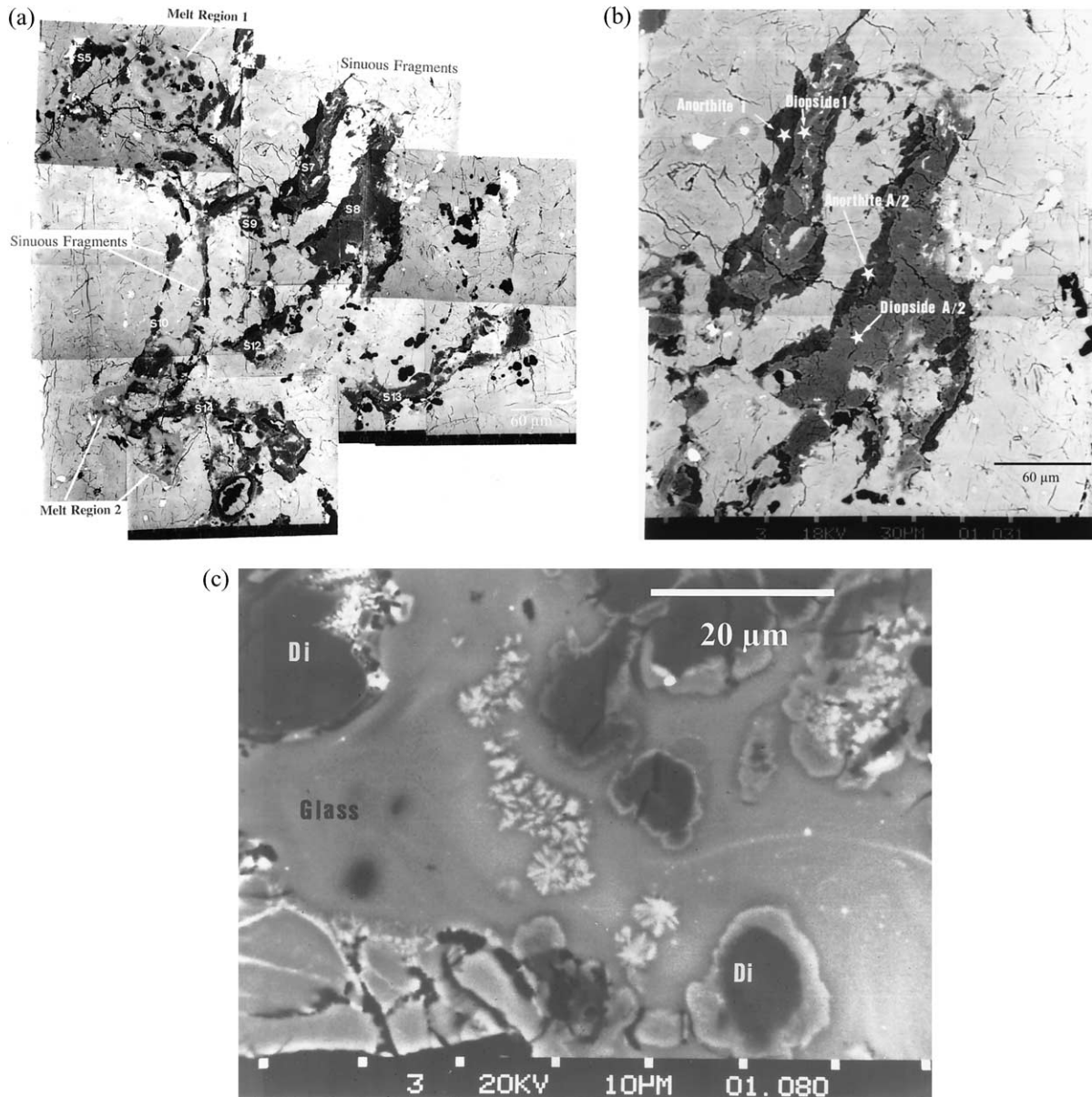
Fig. 5. (a) Detail from the upper left half of Figure 3 depicting 10 of the 14 sinuous inclusions and the melt regions 1 and 2. (b) Enlargement of (a) showing sinuous fragments S7 and S8. The numbers refer to the ion probe Mg isotopic measurements shown in Figure 23a & 24. (c) A detail from melt region 1 in the top of (a) depicting heterogeneous quenched glass with dendritic melilite skeletal crystals (white center) and residual diopside (Di) with melilite envelops (light gray).

2.3. Secondary Ion Mass Spectrometry

Isotopic and trace element analyses were made in situ with the Washington University ion microprobe, a modified CAMECA IMS 3f instrument. Measurement techniques for Mg isotopes and Al/Mg ratios have previously been described by McKeegan et al. (1985) and Fahey et al. (1987a, 1987b). For relative sensitivity factors of Mg and Al, we used those given there. The instrumental mass fractionation F_{Mg} was determined from the $^{25}Mg/^{24}Mg$ ratio by subtracting from the $\Delta^{25}Mg$ value the instrumental mass fractionation of $F_{Mg} = -18.3‰/amu$ measured in terrestrial Burma spinel (USNM #135273). The instrumental mass fractionation of melilite was taken to be the same as that of spinel (Fahey et al., 1987b). Measurement techniques for the isotopic analysis of Ca and Ti were those given by Fahey et al. (1987a), Ireland (1990), and Lundberg et al. (1994).

Trace element measurements were made in the energy-filtering mode (Zinner and Crozaz, 1985). The relative ion yields used are those given by Ireland et al. (1991) for the silicate phases and those of Fahey et al. (1987b) and Ireland et al. (1991) for perovskite. The ion yield of Sc was taken to be that given by (Weber et al., 1995).

3. RESULTS

3.1. Bulk Composition of Efremovka 101

Results of the INAA and the bulk Efremovka sample are presented in Table 1. The comparatively high contents of Fe, Mn, Ni, etc. normally absent from refractory inclusions reflect the presence of bulk Efremovka material in the analyzed sample. The assumption that the contents of Mn, Ni, Co, Au, Se,
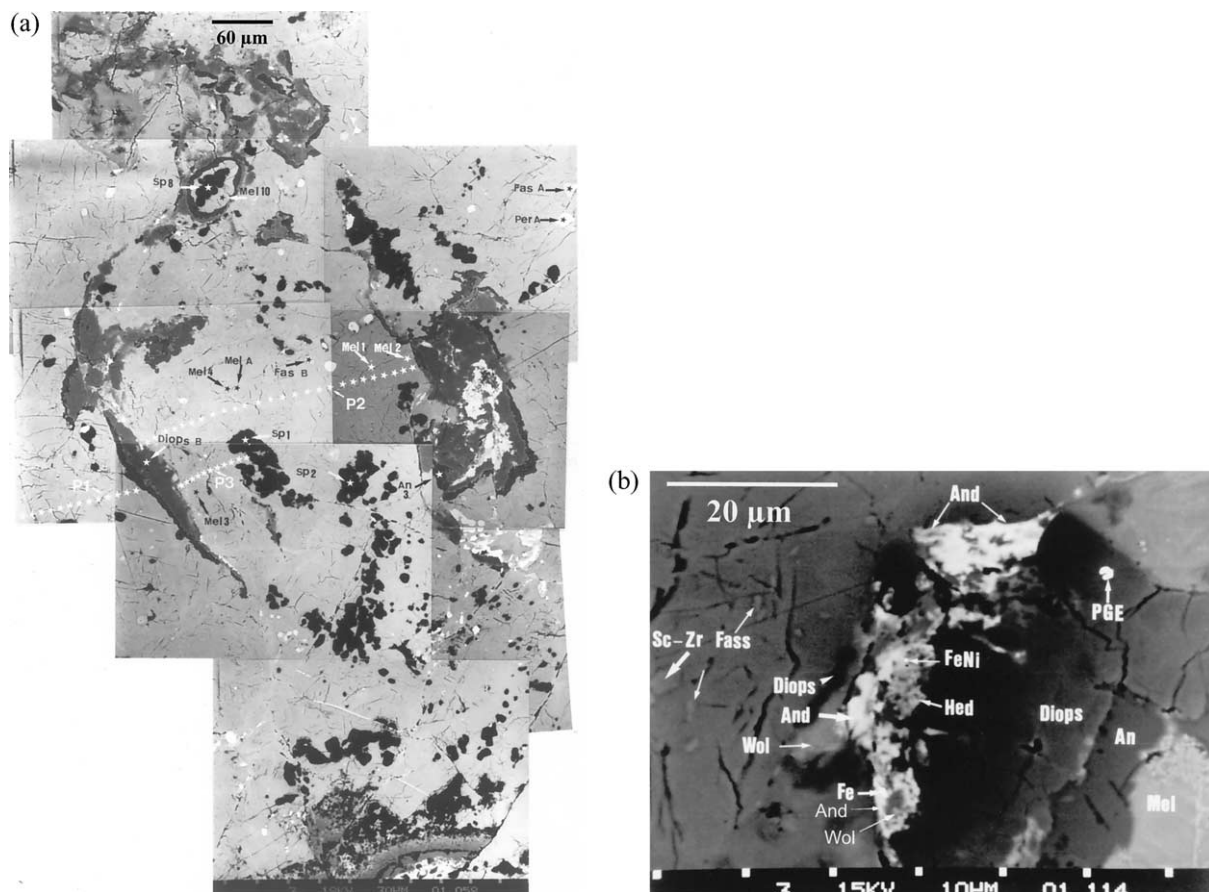
Fig. 6. (a) A back scattered electron mosaic of subinclusions 1 and 2. White aligned stars designate the path of the microprobe profiles across subinclusion 1 (P2) and a portion of the profile from the rim sequence of subinclusion 1 to the rim sequence of 101.1 host (P1), and from the spinel cluster in subinclusion 1 to its rim sequence (P3). Numbers refer to ion probe trace element measurements (Figs. 17 to 20). (b) A detail from the upper part of sinuous fragment 7 (S7 in Fig. 5a) showing an enclave of the assemblage andradite (And)–hedenbergite (Hed)–wollastonite (Wol) entirely confined to the sinuous fragment. Notice the fluffy nature of the intergrowth of andradite and wollastonite (lower center) and a bleb of pure metallic Fe (Fe) between andradite and wollastonite.

and As in the inclusions themselves are negligible leads to an estimated fraction of 41% bulk Efremovka in the analyzed sample. CI-normalized refractory lithophile element (RLE) concentrations of the bulk sample are shown in Figure 1. Correcting for the contribution from bulk Efremovka would increase the enrichment factors by approximately 1.6 but would not significantly change the overall pattern in Figure 1. This pattern is essentially flat with negative anomalies in Eu and Yb. This type of pattern is typical of Group III CAIs as classified by Martin and Mason (1974) and Mason and Martin (1977).

The relative amounts of 101.1, 101.2 and Efremovka matrix were estimated by point counting of the surfaces and then the volumes and inferred masses of the three units in the polished thin section on a petrographic microscope. The bulk composition of the coarse grained inclusion 101.1 was then obtained by subtracting the composition of 101.2 (as obtained from the electron microprobe and secondary-ion mass spectrometry [SIMS] analysis) from that of the bulk sample and by making an additional correction for the estimated "contamination" by bulk Efremovka, using the data in Table 1.

The fine-grained inclusion 101.2 is chemically uniform with

a Group II pattern, as determined with the ion probe. Subtraction of 30% of 101.2 from the bulk 101.1 + 101.2 leads to estimation of the composition of 101.1, which has a superrefractory pattern, complementary to the pattern of 101.2, as shown in Figure 2. Inclusion 101.1 is the larger of the two CAIs. Energy-dispersive spectrometry–SEM analyses indicate that grains of every individual mineral species in the smaller, fine-grained inclusion 101.2 have the same chemical composition. This was confirmed by SIMS analysis also to be the case for trace elements. Measurements of three different spots gave the same trace element patterns within analytical errors (Table 2). The average of these is shown in Figure 2 as open circles. This is a Group II pattern as defined by Martin and Mason (1974). In plotting the patterns in Figure 2, the volatility sequence of the most refractory elements (UR elements) was slightly changed to produce a smooth increase in abundances between Lu and Tb for CAI 101.2. In condensation calculations, Hf, Zr, and Sc condense into separate phases before the REEs (Kornacki and Fegley, 1986). However, since the relationship between activity and composition of Hf, Zr, and Sc in these phases and of the REEs in perovskite, the assumed REE
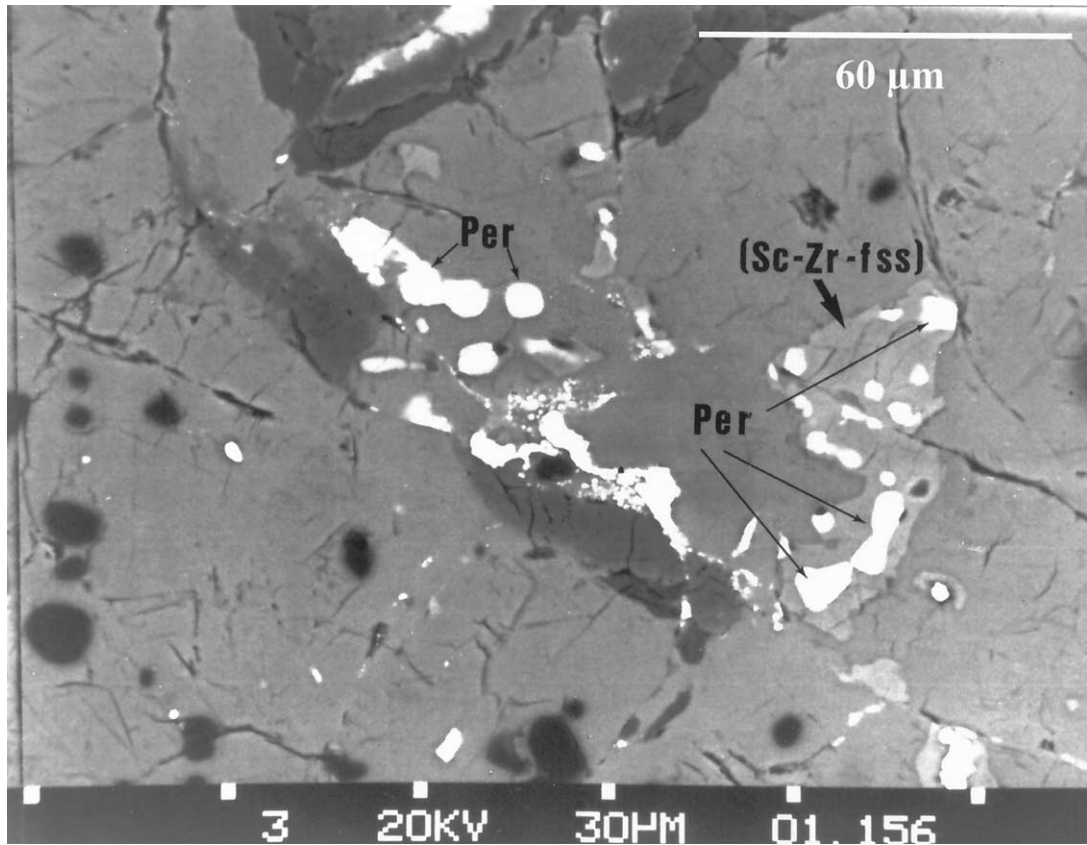
Fig. 7. A back scattered electron detail from Figure 6a showing a whole cluster of perovskite (Per) enclosed in a Sc-Zr-fassaite (Sc-Zr-fss).

host phase, is not known, the true volatility sequence may differ from the calculated sequence (see e.g., Kimura et al., 1993). This is, however, not relevant for further discussion.

The inferred 101.1 pattern displays a comparatively smooth decline in element abundances with increasing volatility (Fig. 2). As we will demonstrate later in more detail, individual phases in 101.1 have higher than chondritic Lu/La ratios, while 101.2 has a much lower ratio, resulting in a chondritic ratio for the bulk sample.

3.2. Petrography

CAI 101.1 is 1.6 mm in diameter and is completely surrounded by a multilayer rim sequence (Fig. 3). It may be classified as a compact Type A CAI (Grossman, 1975). However, the relative abundances of perovskite, fassaite, and spinel as well as their textural relationships to both melilite and metal are different from those observed in typical compact Type A inclusions (Grossman, 1975; Fahey et al., 1987b; MacPherson et al., 1988). The core consists of gehlenitic melilite that constitutes ~80 vol.% of its volume. It also contains sinuous fragments (12% by volume) and refractory fragments consisting of an unusual symplectic intergrowth of Cr-bearing spinel, fassaite, and perovskite. Other minerals encountered are FeNi-metal blebs, Pt-metal nuggets, Y-rich perovskite, Sc- and Zr-rich fassaite, and Fe-free spinel. Spinel, perovskite, and FeNi metal constitute 8% by volume of the core.

Efremovka 101.1 is unique among Type A CAIs. Spinels usually occur in compact clusters, some with framboidal structure, mainly in the right half of the core (Fig. 3). The right half of the core also contains numerous large grains of FeNi-metal and Y-rich perovskite (Fig. 4). More than 14 sinuous fragments are crowded in the left half of the core (Fig. 5a). Partially attached to the sinuous fragments are two oval objects of different sizes, with individual rim sequences (Figs. 3 and 5a). The larger object (hereafter called subinclusion 1 is 350 μm in diameter (Fig. 6a). The smaller object (hereafter called subinclusion 2) is 60 μm in diameter and has a concentric structure.

3.2.1. The Core of the CAI

The core consists of a polycrystalline mosaic of large (up to 450 μm in diameter) individual melilite crystals with no apparent spatial orientation with respect to the rim. Individual spinel clusters are entirely enclosed in separate melilite crystals. Perovskites vary in size between a few microns and 60 μm (Figs. 3, 4, and 7). They are in some cases caught between individual spinel crystals, present inside spinel, or occur in clusters (Fig. 4). Large perovskite grains and large FeNi-metal blebs usually occur together and are intimately intergrown with compact spinel clusters (Fig. 4). Both perovskite and metal are surrounded by rims of Sc- and Zr-rich fassaite (Fig. 4). In some cases, whole clusters of Y-rich perovskite grains are found to be enveloped by single large grains of Sc- and Zr-rich fassaite
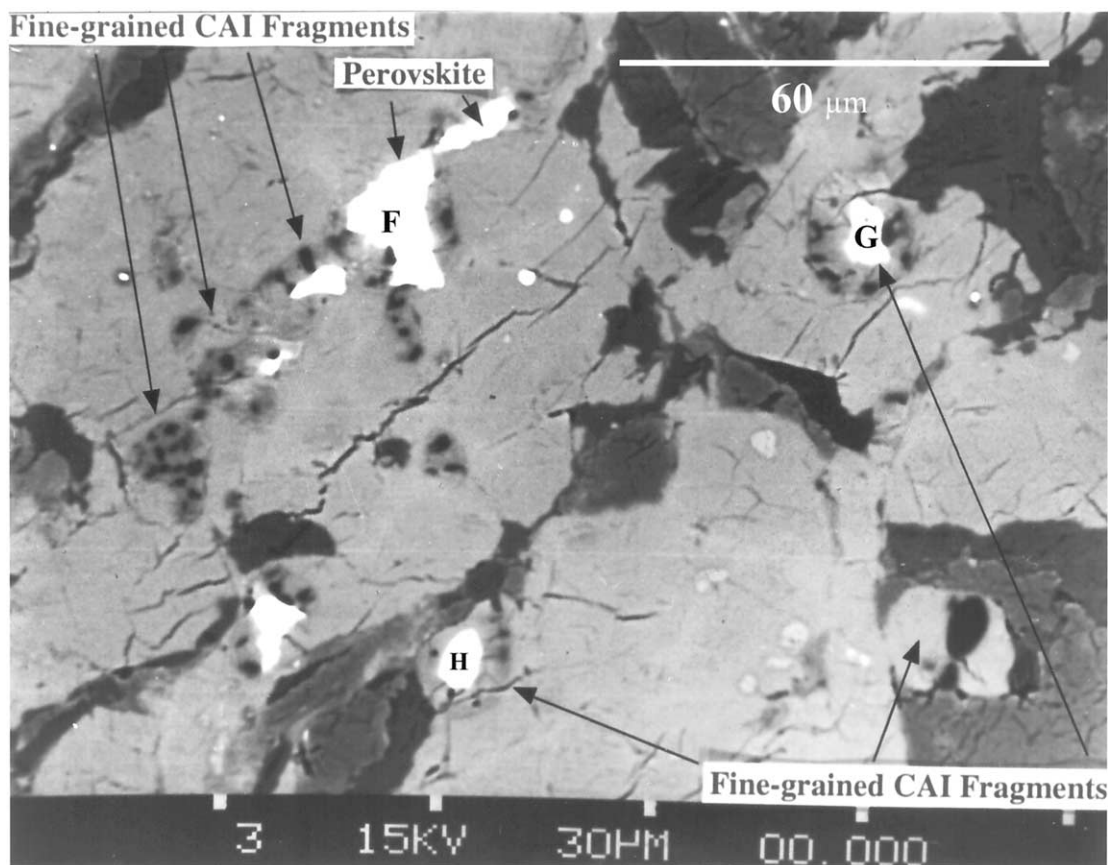
Fig. 8. An accumulation of small Ca-Al-rich inclusion (CAI) fragments consisting of the perovskite cores F, G, and H (see also Figs. 13, 18, and 22), Fe-spinel, Ti-Al-fassaite, and anorthite.

(Fig. 7). Metal, perovskite, and Sc-Zr-fassaite were never found in the interstices of individual melilite crystals, indicating that they were already present before onset of melilite crystallization.

In the left half of the core and adjacent to some sinuous fragments, two melt pockets are present. These areas consist of heterogeneous Al-rich glass in which Fe-rich schlieren occur with numerous skeletal quench crystals of gehlenite and residual rounded diopside grains overgrown by amoeboid layers of gehlenitic melilite (Figs. 5a and 5c).

3.2.2. Sinuous Fragments

The sinuous fragments are roughly aligned parallel to one another, each consisting of two layers with Al-diopside on the concave side and anorthite on the convex side (Fig. 5a). Larger fragments usually have three successive mineral layers of Al-diopside–diopside–anorthite (Figs. 5a and 5b). Adjacent to some of the sinuous fragments are several small fragments consisting of a fine-grained symplectite-like intergrowth of Fe-Cr-spinel, Ti-Al-fassaite, perovskite, and anorthite (e.g., perovskites F, G, and H in Fig. 8). This intergrowth is identical to quench textures found in another CAI from Efremovka, E49 (Zinner and El Goresy, 1994).

Enclaves of oxidation and alteration assemblages consisting of a polycrystalline andradite interior with a corona of wollas-

tonite and hedenbergite occur in the interior of many sinuous fragments (Figs. 5a and 6a). High magnification studies revealed an intimate intergrowth of wollastonite, hedenbergite, andradite and small blebs (~3 μm) of pure Fe metal (Fig. 6b). This assemblage is entirely confined to and entirely sealed off in the interiors of the sinuous fragments (Figs. 5a, 5b, and 6b). The texture of this assemblage is strongly suggestive of reduction of andradite and hedenbergite to wollastonite + pure metallic Fe. Melilite in the core of the CAI, and the rim sequences are devoid of any alteration or alteration veins.

3.2.3. Subinclusions

The core of subinclusion 1 consists of gehlenitic melilite, with several spinel clusters, Y-rich perovskite, Sc-Zr-fassaite, and FeNi-metal blebs (Figs. 5a and 6a). It is surrounded by an almost complete rim sequence with a layering arrangement similar to that of the sinuous fragments (Fig. 5b). Offset faults similar to those present in the outer rim of the host CAI are also present (Fig. 6a). Enclaves of the andradite–hedenbergite–wollastonite–pure Fe metal assemblage are also found inside of the thick diopside layer. Between the rim sequence of the subinclusion and its core is an almost continuous thin layer of a Fe-bearing silicate glass (~2 μm). This layer is in the BES mode brighter than melilite, sharply bounded from it, and chemically heterogeneous.
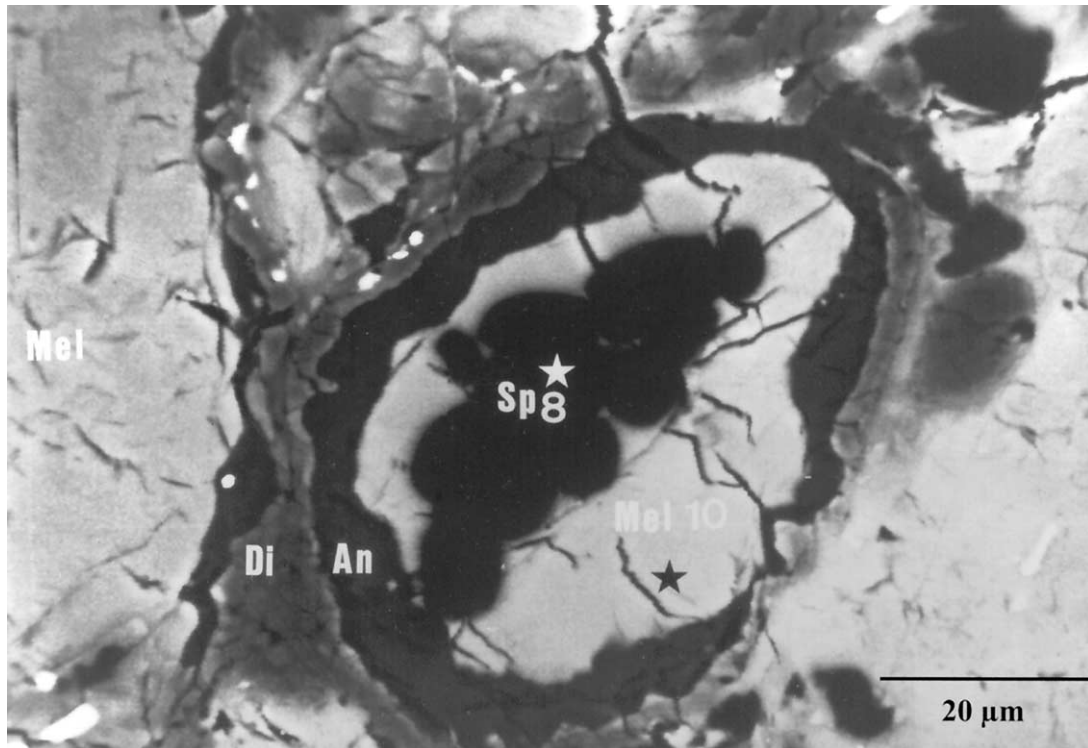
Fig. 9. Subinclusion 2 consisting of a dense spinel core covered by successive layers of gehlenitic melilite, anorthite (An), and diopside (Di).

Subinclusion 2 is only 60 μm in diameter and has a perfectly concentric structure with a closely packed spinel core (Fig. 9). This core is covered with three layers consisting of (from the inside outward) gehlenitic melilite (Ak_{10}-Ak_{15}), anorthite, and diopside.

3.2.4. Rim Sequence of the Host CAI

The rim sequence consists of the following units (from the inside out [Figs. 3 and 10a]): (a) A compact layer of Fe-poor spinel with variable thickness (10 to 30 μm). In some areas, spinel grains have accumulated into compact rounded clumps of up to 50 μm in diameter; (b) a discontinuous thin layer (~5 μm) of Sc-Zr-fassaite; (c) a layer of Al-diopside; (d) a layer consisting of individual grains of forsteritic olivine ($Fo_{96.3}$-Fo_{99}); (e) a layer of pure diopside; and (f) in a few regions, the diopside layer is covered by a discontinuous layer of olivine or by thick clumps of closely packed olivine crystals (Fo_{93}-Fo_{99}) next to the matrix (Fig. 10b). The forsterite clumps contain very small bright blebs and patches consisting of iron sulfide and an iron-rich silicate, presumably fayalitic olivine, in the interstices of the individual olivine crystals. A layer of fine-grained fayalitic olivine surrounds the clumps. There exists a perfect match between the crystal surfaces of neighboring diopside grains in layers 3 and 5 and of olivine grains in layers 4 and 6 (Fig. 10a). This texture looks deceptively like a triple junction, characteristic of recrystallisation during annealing. However, it is quite distinct from the latter, in that the crystal surfaces of all neighboring grains in the same or adjacent layers are separated by open joints (Fig. 10a). Offset faults are abundant, a feature

characteristic also of other Efremovka CAIs (Fahey et al., 1987b). The rim sequence does not contain any melilite, perovskite, hibonite, or secondary alteration phases and is hence quite different from those described before in Allende CAIs (Wark and Lovering, 1977; 1986; MacPherson et al., 1981, 1988). Cracks and faults in melilite in contact with the rim sequence or with the Efremovka matrix are empty, with no alteration or oxidation products filling them.

3.3. Mineral Chemistry

3.3.1. Host CAI and Subinclusions

Melilite. Melilite analyses were made in all lithological units of Efremovka 101.1. They include one profile across the host inclusion, two profiles across subinclusion 1, and measurements in subinclusion 2 (Table 3). Figure 11 displays histograms of the melilite compositions in the profiles across the host CAI, subinclusion 1, and in subinclusion 2. The ranges of melilites compositions differ among the analyzed objects: (a) Compositions in the core of the host CAI span a narrow range from $Åk_{19}$ to $Åk_{31}$, (b) those in subinclusion 1 have a wider range from $Åk_6$ to $Åk_{27}$, and (c) melilites in subinclusion 2 are even more gehlenitic and display a very narrow range ($Åk_9$ to $Åk_{14}$).

Compositions along the traverses of the host CAI show only slight fluctuations except for an abrupt descent from $Åk_{28}$ to $Åk_{23}$. Close to the rim sequence of the host CAI, there is a remarkable decrease in the Åk content, reaching a minimum of $Åk_{19}$ at the contact to the spinel layer of the rim. A few melilite
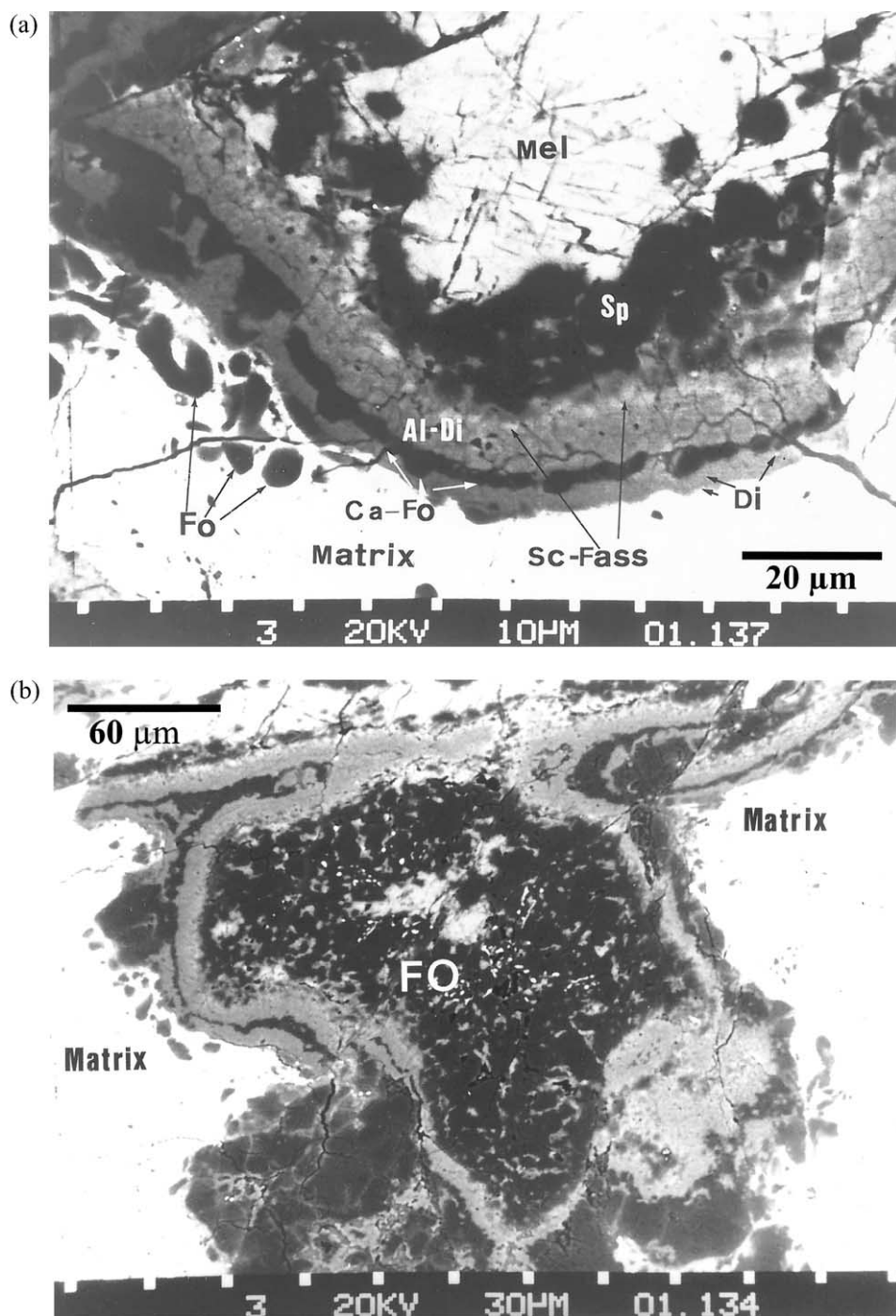
Fig. 10. (a) Detail of the rim sequence of the host Ca-Al-rich inclusion (CAI) depicting the successive rim layers from inside out: layer 1 spinel (Sp), layer 2 Sc-rich fassaite (Sc-Fass), layer 3 Al-diopside (Al-Di), layer 4 Ca-olivine (Ca-Fo), layer 5 diopside (Di), and layer 6 forsterite (Fo). (b) Detail from an outer region of the rim sequence of the host CAI depicting forsterite clumps in layer 6.

analyses in the host CAI and the subinclusions revealed detectable concentrations of Y_2O_3 (0.05 to 0.14 wt.%).

Spinel. Individual spinel grains were analyzed in one cluster in the core of the host CAI, in two clusters in subinclusions 1, in the core of subinclusion 2, and in several sections of layer 1 of the rim sequence of the host CAI. There are distinct differences in the V_2O_3 and Cr_2O_3 contents among the various spinel

units in the core and between the spinels in the core and those in the rim sequence (Fig. 12a). Spinels from the cluster in the host CAI have high V_2O_3 (0.93 to 1.11 wt.%) and low Cr_2O_3 (0.12 to 0.20 wt.%) contents. The two clusters in subinclusion 1 have different V_2O_3 and Cr_2O_3 contents (Fig. 12a). In the first cluster, V_2O_3 and Cr_2O_3 contents vary between 0.56 and 1.05 wt.% and 0.13 and 0.38 wt.%, respectively (line A in Fig. 12a).

Table 3. Chemical compositions of melilite in the core of 101.1 and in the captured subinclusions (wt. % and cation number) as measured by electron microprobe.

Oxide	Core 1	Core 2	Subinclusion 1	Subinclusion 1	Subinclusion 1[a]	Subinclusion 2	Subinclusion 2
MgO	2.70	4.66	0.80	4.01	5.32	1.24	2.10
Al_2O_3	31.1	25.4	34.4	26.6	25.7	33.1	31.2
SiO_2	25.3	28.9	23.4	27.4	29.3	23.5	24.8
CaO	39.5	40.5	40.5	40.9	36.5	41.1	39.4
TiO_2	<0.01	<0.02	0.04	0.05	1.43	<0.01	0.02
V_2O_3	<0.02	n.d.	n.d.	n.d.	0.04	n.d.	n.d.
Cr_2O_3	n.d.	<0.02	<0.02	n.d.	0.03	<0.01	<0.01
MnO	n.d.	n.d.	0.02	n.d.	n.d.	0.02	0.03
FeO	0.11	0.01	0.04	n.d.	0.88	n.d.	0.04
ZnO	n.d.	n.d.	n.d.	0.05	0.03	0.03	n.d.
Total	98.70	99.46	99.20	99.01	99.23	98.99	97.59
Number of cations per formula unit							
Mg	0.185	0.316	0.054	0.274	0.359	0.085	0.145
Al	1.684	1.368	1.861	1.445	1.375	1.802	1.714
Si	1.165	1.321	1.076	1.262	1.330	1.086	1.154
Ca	1.945	1.984	1.995	2.020	1.776	2.032	1.966
Ti	0.000	0.000	0.000	0.001	0.048	0.000	0.000
V	0.000	0.000	0.000	0.000	0.001	0.000	0.000
Cr	0.000	0.000	0.000	0.000	0.002	0.000	0.000
Mn	0.000	0.000	0.000	0.000	0.000	0.000	0.000
Fe	0.004	0.000	0.001	0.000	0.033	0.000	0.001
Zn	0.000	0.000	0.000	0.001	0.000	0.000	0.000
Total	4.983	4.989	4.987	5.003	4.922	5.005	4.980
Åk	19.9	31.4	6.54	27.9		8.9	14.5

n.d. = not detected.
[a] Glass.

Data points of the second cluster plot in an area with a narrow compositional range (0.61 to 0.82 wt.% V_2O_3 and 0.11 to 0.20 wt.% Cr_2O_3). Spinels in the core of subinclusion 2 define a population with moderate V_2O_3 and high Cr_2O_3 contents (0.50 to 0.64 wt.% V_2O_3 and 0.37 to 0.54 wt.% Cr_2O_3) that is well separated from all other populations (line B in Fig. 12a). The Cr_2O_3/V_2O_3 correlations A and B suggest crystal/liquid fractionation of V and Cr during crystallization. Inspection for a V_2O_3-vs.-TiO_2 correlation in the first spinel cluster of subinclusion 1 revealed the presence of two distinct populations. Spinels occupying the core of this cluster have high V_2O_3 contents, and the data points are aligned on an array with a negative V_2O_3-vs.-TiO_2 correlation, while the spinels occupying the outer regions have lower V_2O_3 and TiO_2 contents and plot along an array with a positive slope (Fig. 12b) (see discussion). There is no apparent V_2O_3-vs.-TiO_2 correlation for spinels in subinclusion 2 (Fig. 12b), host CAI, rim sequence, and in the second cluster in subinclusion 1. All spinels studied are low in TiO_2 (0.04 to 0.38 wt.%). Spinels in the core have low FeO (0.03 to 0.29 wt.% FeO), while those in the rim sequence generally have higher FeO concentrations (0.05 to 4.11 wt.%). The FeO enrichment probably resulted from a later oxidation process before incorporation of the CAI into the Efremovka matrix.

Perovskite. We measured Ca, Ti, and the minor elements Al, Mg, Si, V, Zr, Y, Nb, and Sc in 76 grains (see analytical procedure). Totals of all analyses ranged from 97.07 to 100.2% depending on the grain size, with small ($\sim$5 μm) grains tending to have lower totals. All perovskites show high concentrations either in one, two, or all three of the oxides ZrO_2, Y_2O_3, Sc_2O_3 (<0.02 to 1.13 wt.% ZrO_2; 0.18 to 1.38 wt.% Y_2O_3; and <0.02 to 0.40 wt.% Sc_2O_3). Abundances of ZrO_2, Y_2O_3, Sc_2O_3,
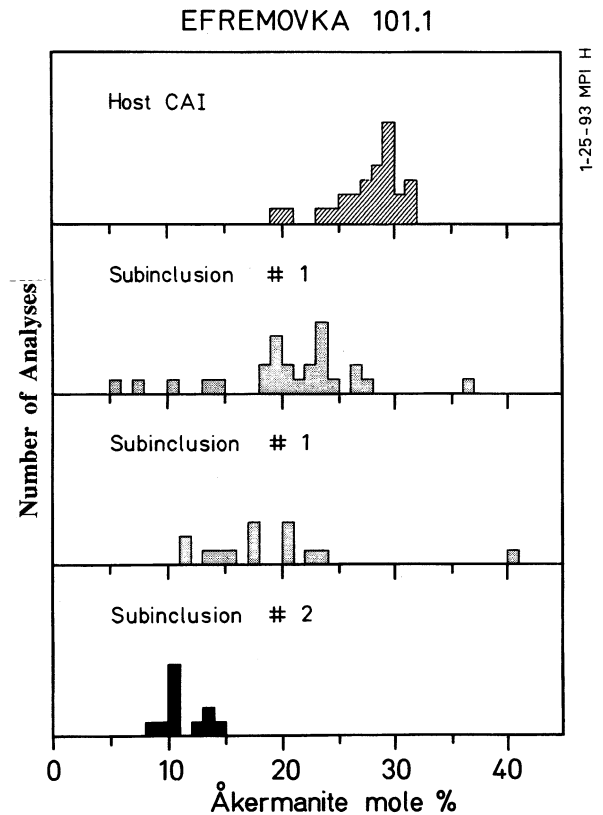

Fig. 11. Histograms of melilite compositions (expressed as åkermanite contents) in the host Ca-Al-rich inclusion (CAI) and subinclusions 1 and 2.
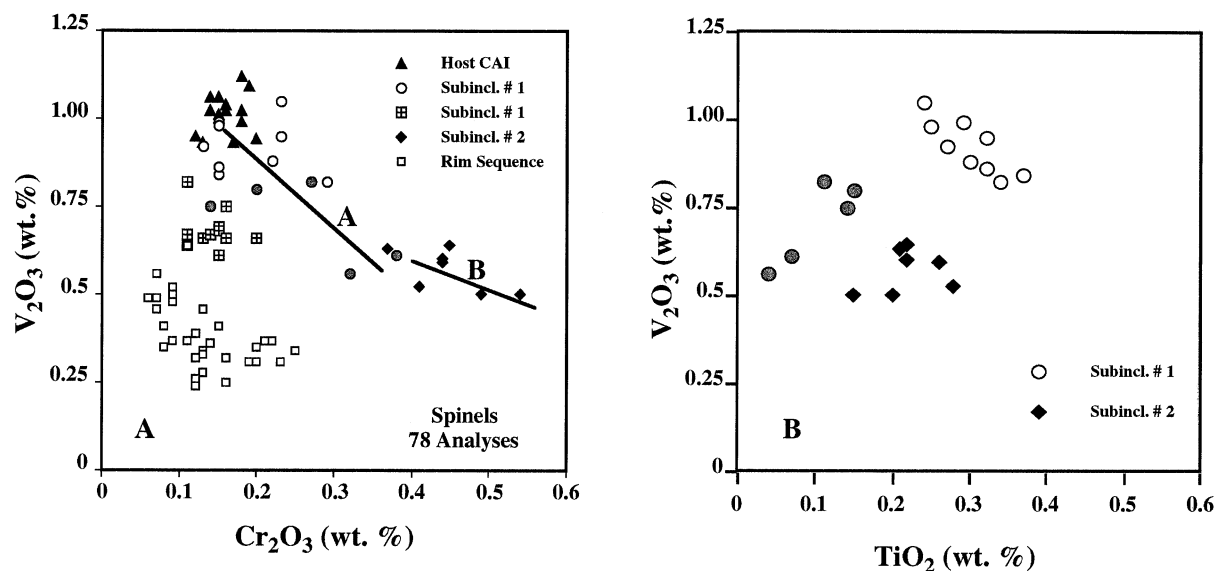
Efremovka 101.1

Fig. 12. (a) V_2O_3 versus Cr_2O_3 contents of various spinel clusters in the host Ca-Al-rich inclusion (CAI), subinclusions 1 and 2, and the rim sequence of the host CAI. (b) V_2O_3 vs. TiO_2 contents of first spinel cluster in subinclusion 1 (line A in [a]) and spinels in subinclusion 2. Spinels from core (open circles) and outer regions (filled circles) of the cluster in subinclusion 1 have distinct V_2O_3-vs.-TiO_2 relationships.
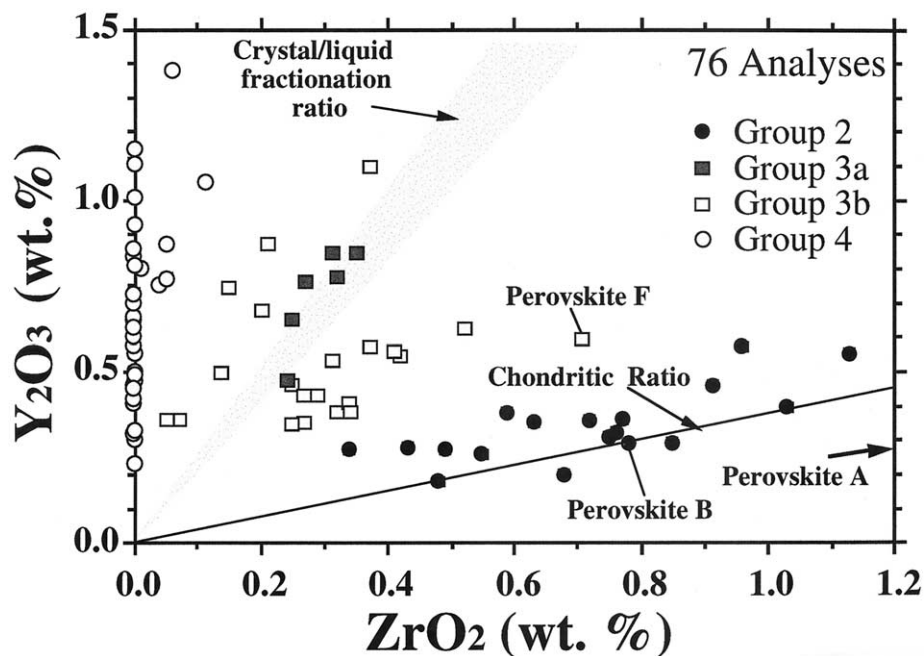

Fig. 13. Y_2O_3 vs. ZrO_2 contents of 76 perovskites in the host Ca-Al-rich inclusion and subinclusion 1. We can distinguish three perovskite groups with different Y_2O_3/ZrO_2 ratios.

V_2O_3, and Nb_2O_5 vary considerably, in a systematic manner, among many grains. Exceptions from this observation are perovskites F, G, and H (Fig. 8) in symplectitic CAI fragments (see section 3.2.2) that have relatively high Nb concentrations (see section 3.4). Perovskites in the studied units contain quite variable amounts in V_2O_3 (0.39 to 1.13 wt.%), SiO_2 (0.05 to 0.64 wt.%), MgO (<0.01 to 0.87 wt.%), and Al_2O_3 (0.12 to 3.89 wt.%).

Several perovskite populations with different Y_2O_3/ZrO_2 ratios can be recognized (Fig. 13) (see discussion): (a) Grains with chondritic ratios (0.364 wt.%; Anders and Grevesse, 1989; group 2 in Fig. 13; analyses 1 and 2 in Table 4). Twenty-five

percent of the analyzed grains belong to this category; (b) perovskites with ratios between 0.83 and 7.5. This group in turn consists of two subgroups: 6 perovskites (8%; group 3a in Fig. 13; analyses 3 and 4 in Table 4) have Y_2O_3/ZrO_2 ratios close to those obtained from crystal/liquid fractionation experiments (2.07 in air and 2.59 at low f_{O_2}; Simon et al., 1994), and 21 perovskites of this group fall outside this narrow range (group 3b; Fig. 13); and (c) perovskites with very high Y_2O_3 (up to 1.38 wt.%) and very low ZrO_2 (<0.10 wt.%) contents are members of group 4 (see analyses 5 and 6 in Table 4). This group comprises 40% of the analyzed grains. Perovskites of this group are too small (<10 μm) to be cleanly analyzed in the ion probe. Ion probe measurements revealed an additional but rare group (group 1) with Y_2O_3/ZrO_2 ratios lower than chondritic (see section 3.4).

Many perovskites have moderate amounts of Ti^{3+} (up to 7.2 mol.%). The presence of and variation in Ti^{3+} is considered to reflect a coupled substitution of the type $R^{3+} + Ti^{3+} \Rightarrow Ca^{2+} + Ti^{4+}$ (Simon et al., 1994) (R^{3+} stands for $REE^{3+} + Y^{3+}$). However, we find a more complex coupled substitutional relationship whereby several R^{3+} cations ($Y^{3+} + Sc^{3+} + Al^{3+} + Ti^{3+} + V^{3+}$) are substituting for R^{2+} ($Ca^{2+} + Mg^{2+}$) + R^{4+} ($Ti^{4+} + Zr^{4+} + Si^{4+}$) cations. The results are shown in Figure 14. All data points plot on a tight linear array intersecting the abscissa at 2.00 total cations, thus strongly supporting the applied Ti^{3+} calculation procedure and the proposed coupled substitutional scheme.

Fassaite. A total of 232 grains and reaction rims around perovskite and FeNi metal blebs were analyzed. Some of the analyzed grains were found to contain enormous concentrations of Sc_2O_3 (up to 12.9 wt.%; analysis 7 in Table 5), ZrO_2 (up to 5.38 wt.%; analysis 8 in Table 5), and V_2O_3 (up to 5.32 wt.%). Variations in TiO_2, Sc_2O_3, ZrO_2, V_2O_3, Y_2O_3, and Al_2O_3 are considerable and follow distinct systematics (see below). The concentration ranges for these oxides are (in wt.%) 7.86 to 18.0 TiO_2, 0.24 to 12.9 Sc_2O_3, <0.01 to 5.38 ZrO_2, 0.45 to 5.32 V_2O_3, <0.02 to 0.13 Y_2O_3, and 19.3 to 25.6 Al_2O_3. In addition, the calculated Ti^{3+}/Ti^{tot} ratios vary between 0.27 and 1. The Sc_2O_3 and ZrO_2 concentrations are positively correlated with a correlation coefficient of 0.88 (Fig. 15a). More will be said about the origin of this correlation in the discussion.

The Sc_2O_3/ZrO_2 correlation is not strictly linear, and its slope slightly decreases at higher Sc_2O_3 and ZrO_2 concentrations (Fig. 15a). This correlation reflects a complex coupled substitution involving Mg, Ti, Sc, Zr, V, and Al. This is demonstrated by the good correlation between $Mg^{2+} + Ti^{4+}$ and $Sc^{3+} + Zr^{4+} + Ti^{3+} + V^{3+}$, satisfying the equation $y = 0.70 - 0.66x$ with a linear regression coefficient of 0.84 (Fig. 16). Components involved in these substitutions are the Ca_{Ts} ($CaAl_2SiO_6$), T_4P ($CaTi^{4+}Al_2O_6$), the Sc and Zr clinopyroxene components ($CaSc^{3+}AlSiO_6$), and ($CaZr^{4+}Al_2O_6$) (Lindstrom, 1976; Dunn and McCallum, 1982; Beckett, 1986; Colson et al., 1989; Gallahan and Nielsen, 1992), and additional molecules involving Ti^{3+}, such as ($CaTi^{3+}AlSiO_6$), ($CaSc^{3+}Ti^{3+}SiO_6$), and ($CaZr^{4+}Ti^{3+}AlO_6$) in competition with the Ca_{Ts} and T_4P molecules. The large variations in Ti^{3+} contents encountered here cannot have resulted from intrinsic variations in f_{O_2} in the CAI liquid. The variations rather reflect the preference of the growing fassaite crystal for Ti^{3+} over Ti^{4+} (Beckett, 1986) also with increasing contents of Sc^{3+}, Zr^{4+}, and V^{3+}.

Microprobe profiles across fassaite rims around FeNi metal blebs and around perovskite grains indicate contrasting zoning behavior in the concentrations of Sc_2O_3, ZrO_2, and V_2O_3. Both Sc_2O_3 and ZrO_2 contents increase from the contact of the fassaite with the FeNi metal core to the outer rim (e.g., from 3.07 to 6.55 wt.% Sc_2O_3 and from 1.73 to 4.23 wt.% ZrO_2). V_2O_3 decreases along the same path (from 2.51 to 1.80 wt.%; analyses 1 and 2 in Table 5). In contrast, the concentrations of the three oxides display exactly the opposite trends in fassaite rims around perovskite grains (e.g., from 11.4 to 8.97 wt.% Sc_2O_3, from 4.27 to 3.70 ZrO_2, and from 2.14 to 2.36 wt.% V_2O_3; analyses 3 to 6 in Table 5). The observation that fassaite rims around FeNi metal blebs become increasingly enriched in Sc_2O_3 and ZrO_2 from the metal contact to the rim strongly suggests growth from a liquid with increasing concentrations in these oxides (hereafter called normal trend). The zoning trends of Sc_2O_3 around FeNi metal blebs are reverse to those reported by Simon et al. (1991) in subliquidus fassaites from three Type B inclusions. Evidently, fassaite rims around FeNi in Efremovka must have gained considerable amounts of V_2O_3 from the metal core because of preferential oxidation of vanadium during cooling of the CAI liquid and during subsequent subsolidus equilibration. In contrast, the decrease in Sc_2O_3 and ZrO_2 in fassaites from the contact with the perovskite cores outward (hereafter called reverse trend) is presumably the re-

Table 4. Chemical compositions of perovskites in the core of 101.1 and in the captured subinclusion 1 (wt. % and cation number) as measured by electron microprobe.

| Oxide	Group 2	Group 2	Group 3	Group 3	Group 4	Group 4
CaO	40.2	39.2	38.2	38.3	38.4	38.7
TiO_2	57.2	57.4	57.8	57.6	58.4	58.0
SiO_2	0.17	0.48	0.22	0.22	0.17	0.14
V_2O_3	0.85	0.70	0.79	0.74	0.79	0.83
Y_2O_3	0.55	0.29	0.84	0.84	1.01	1.38
Sc_2O_3	0.09	0.11	n.d.	n.d.	<0.01	0.04
ZrO_2	1.13	0.85	0.35	0.31	n.d.	0.06
Cr_2O_3	<0.02	n.d.	<0.01	<0.01	<0.01	0.04
Al_2O_3	0.32	0.32	0.33	0.38	0.30	0.16
Na_2O	<0.02	<0.01	<0.02	<0.02	<0.02	<0.02
FeO	<0.01	0.06	0.03	0.03	0.03	0.10
MnO	<0.01	<0.01	n.d.	n.d.	n.d.	<0.02
MgO	<0.02	0.04	<0.02	<0.02	<0.02	<0.02
Total	100.53	99.45	98.56	98.42	99.10	99.45
Number of cations per formula unit						
Ca	0.977	0.963	0.949	0.949	0.957	0.954
Ti^{4+}	0.963	0.945	0.944	0.944	0.955	0.955
Ti^{3+}	0.012	0.045	0.065	0.065	0.050	0.049
Si	0.030	0.011	0.005	0.005	0.003	0.003
V	0.015	0.013	0.014	0.014	0.014	0.015
Y	0.006	0.003	0.010	0.010	0.012	0.016
Sc	0.001	0.002	0.000	0.000	0.000	0.006
Zr	0.012	0.009	0.003	0.003	0.000	0.000
Cr	0.000	0.000	0.000	0.000	0.000	0.000
Al	0.009	0.008	0.009	0.009	0.008	0.004
Na	0.001	0.000	0.000	0.000	0.000	0.000
Fe	0.000	0.000	0.000	0.000	0.000	0.001
Mn	0.000	0.000	0.000	0.000	0.000	0.000
Mg	0.000	0.000	0.000	0.000	0.000	0.000
Total	2.026	1.998	1.999	1.999	1.999	2.003
Ti^{3+}/Ti^{tot}	1.27%	4.65%	6.84%	6.48%	4.98%	4.92%

n.d. = not detected.

Efremovka 101.1 Perovskites
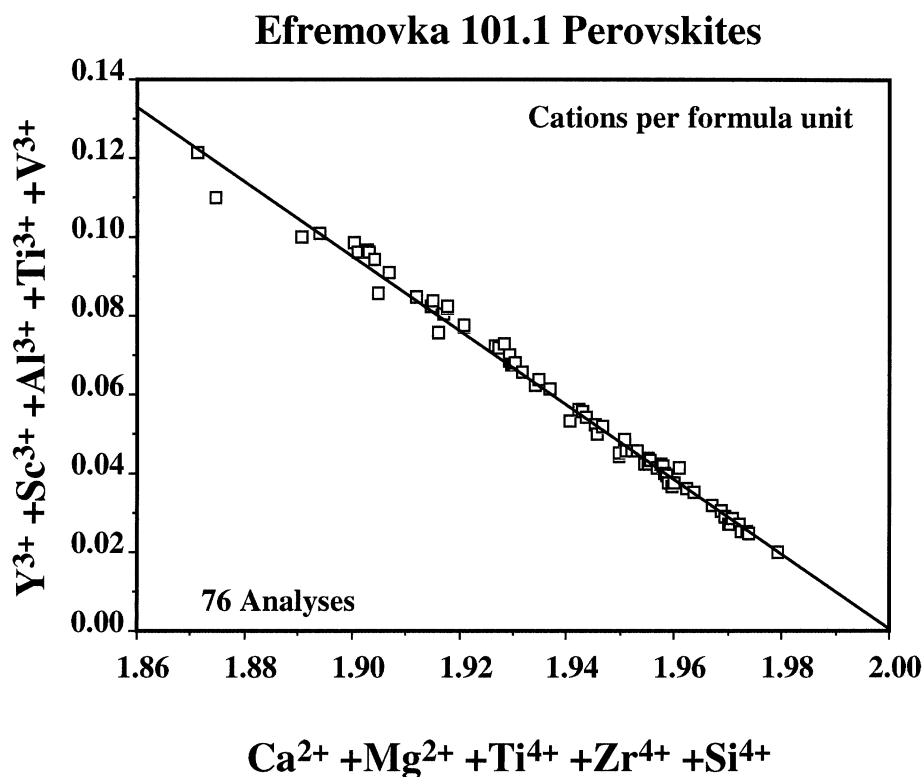
Fig. 14. A plot displaying the (Y^{3+} + Sc^{3+} + Al^{3+} + Ti^{3+} + V^{3+}) vs. (Ca^{2+} + Mg^{2+}) + R^{4+} (Ti^{4+} + Zr^{4+} + Si^{4+}) cation substitutional relationship in perovskites from Efremovka 101.1.

sult of the preferential partitioning of Sc and Zr into the pyroxene structure in comparison to perovskite. Since both assemblages occur close to one another (<60 μm; e.g., Fig. 4), the reverse ZrO_2 and Sc_2O_3 concentration trend could not have resulted from the lack of chemical homogeneity in the cooling liquid on a small scale but rather is due to solid-state diffusion of Sc and Zr from perovskite to the growing fassaite rim during its crystallization and subsequently during cooling after solidification of the CAI. Subsolidus equilibration of the fassaite rim with perovskite might have overprinted a possibly preexisting normal zoning trend. Examples of fassaite analyses displaying the contrasting compositional variations are given in Table 5.

3.3.2. Sinuous Fragments

Diopside. A total of 20 analyses were conducted in the sinuous fragments and in subinclusion 1. Both diopside and Al-diopside show remarkably low TiO_2 (0.03 to 0.35 wt.%) and V_2O_3 (0.01 to 0.14 wt.%) concentrations. There is a continuous increase in the Al_2O_3 content from 0.06 wt.% in the center of the sinuous fragments to 5.25 wt.% at the contact with the anorthite layer or with the melilite of the host. FeO contents vary between 0.06 and 1.70 wt.%. Examples of diopside and Al-diopside analyses are given in Table 6.

Andradite and wollastonite. Analyses were performed on the mineral assemblage in subinclusion 1 and the sinuous fragments. Because of the very small grain size (<2 μm) and the fluffy nature of these phases (Fig. 6b), it was impossible to obtain analyses with totals approaching 100% for andradite,

hedenbergite, or wollastonite. The totals for andradite range from 90.1 to 92.8 wt.% and those for wollastonites from 92.4 to 94.8 wt.%. However, the calculated number of cations for each mineral satisfies the pertinent structural formula. We cannot exclude the possibility that some minor elements in the andradite and wollastonite analyses (Table 7) originated from the neighboring hedenbergite and diopside because of beam overlap.

Anorthite. A total of 333 analyses were conducted on anorthites in all sinuous fragments. The majority of the analyses indicate almost pure anorthite with traces of Na_2O, MgO, and K_2O (<0.08 wt.%). Some 34 analyses revealed, however, relatively high Na_2O contents between 0.27 and 8.47 wt.%. In these analyses, the Na_2O contents positively correlate with deviations from stoichiometry (excess in the number of cations per formula unit). This indicates that the measured Na_2O is not incorporated into the anorthite structure but rather is due to submicroscopic, finely dispersed interstitial Na-bearing phases not resolved in the high magnification SEM photographs (see also MacPherson and Davis, 1993).

3.3.3. Rim Sequence

Spinel (layer 1). Thirty-six analyses were obtained in two different but not adjacent areas of the rim sequence. The spinels have low Zn (ZnO $<$ 0.10 wt.%), reflecting the refractory nature of the rim sequence and indicating that no volatile elements were added during its formation and subsequent oxidation. Concentrations of the minor elements are very low:

Table 5. Chemical compositions of fassaites in the core of 101.1 and in captured subinclusion 1 (wt. % and cation number) as measured by electron microprobe.

Oxide	1	2	3	4	5	6	7	8
CaO	23.9	23.4	23.3	23.4	23.3	23.3	23.2	22.1
TiO_2	12.9	10.5	8.39	9.28	9.03	9.23	11.0	14.6
SiO_2	31.6	29.7	27.8	28.7	28.5	27.6	26.8	24.5
V_2O_3	2.5	1.80	2.14	2.42	2.43	2.36	1.39	1.58
Y_2O_3	0.04	n.d.	0.09	0.04	0.07	0.07	0.04	0.11
Sc_2O_3	3.07	6.55	11.4	9.27	9.68	8.97	12.9	8.20
ZrO_2	1.73	4.23	4.27	4.00	3.80	3.70	4.88	5.38
Cr_2O_3	0.04	0.03	<0.02	0.06	0.07	0.02	0.02	0.07
Al_2O_3	20.0	19.4	20.26	19.4	20.0	20.0	20.7	<0.02
Na_2O	<0.01	<0.02	n.d.	n.d.	n.d.	n.d.	<0.02	22.3
FeO	0.21	0.12	n.d.	n.d.	0.04	n.d.	0.03	0.11
MnO	n.d.	n.d.	n.d.	n.d.	n.d.	n.d.	n.d.	<0.01
MgO	5.50	5.20	3.04	3.46	3.10	3.29	1.79	3.11
Total	101.49	100.90	100.69	100.03	100.02	98.54	102.85	102.06
Number of cations per formula unit								
Ca	0.984	0.977	0.985	0.995	0.991	1.003	0.978	0.938
Ti^{4+}	0.059	0.045	0.000	0.000	0.000	0.028	0.000	0.053
Ti^{3+}	0.305	0.262	0.250	0.276	0.269	0.258	0.324	0.379
Si	1.214	1.159	1.101	1.142	1.133	1.108	1.056	0.970
V	0.077	0.058	0.067	0.077	0.077	0.075	0.043	0.500
Y	0.000	0.000	0.001	0.000	0.001	0.001	0.000	0.001
Sc	0.103	0.222	0.391	0.320	0.334	0.314	0.441	0.282
Zr	0.031	0.080	0.081	0.077	0.073	0.072	0.093	0.103
Cr	0.000	0.000	0.000	0.001	0.001	0.000	0.000	0.001
Al	0.906	0.892	0.944	0.907	0.935	0.949	0.958	1.036
Na	0.000	0.001	0.000	0.000	0.000	0.000	0.001	0.001
Fe	0.005	0.003	0.000	0.000	0.001	0.000	0.000	0.003
Mn	0.000	0.000	0.000	0.000	0.000	0.000	0.000	0.000
Mg	0.314	0.301	0.178	0.204	0.183	0.197	0.104	0.182
Total	3.998	3.998	3.999	3.999	3.998	3.997	3.998	3.999
Ti^{3+}/Ti^{tot}	83.8%	86.2%	100%	100%	100%	92.81%	100%	87.73%

Analyses 1 and 2 are in fassaite around FeNi metal core; 3 to 6 in fassaite around a perovskite core; 7 and 8 fassaites with the highest detected Sc_2O_3 and ZrO_2, respectively.

n.d. = not detected.

0.14 to 0.35 wt.% CaO, 0.10 to 0.37 wt.% TiO_2, 0.07 to 0.25 wt.% Cr_2O_3, and 0.24 to 0.64 wt.% V_2O_3. Spinel compositions in the rim sequence occupy a field with the lowest V_2O_3 and Cr_2O_3 contents (0.24 to 0.64 wt.% V_2O_3 and 0.07 to 0.25 wt.% Cr_2O_3), indicating that these spinels originated from a source genetically unrelated to the spinels in the host CAI (Fig. 12a). They also display a larger variation in their FeO contents (0.05 to 5.4 wt.%) than those in the host.

Sc-bearing fassaite (layer 2). Only nine analyses were made. ZrO_2 and Y_2O_3 contents were not measured because of the lack of probe standards at the time of analysis. However, the concentrations of Zr and Y, along with other trace elements, were measured by SIMS (see section 3.4). The concentrations of TiO_2, Al_2O_3, and V_2O_3 vary in a similar manner as in the Sc- and Zr-rich fassaites of the host CAI. However, the compositional ranges are much narrower. The ranges of these oxides are (in wt.%) 3.51 to 12.3 TiO_2, 13.4 to 24.5 Al_2O_3, and 0.18 to 0.82 V_2O_3 (Table 8). Sc_2O_3 contents are much lower (0.05 to 0.77 wt.%) than in fassaites in the host CAI. All analyses revealed appreciable amounts of FeO (0.59 to 1.89 wt.%).

Diopside (layers 3 and 5). Totals of 14 and 27 analyses were obtained on diopsides in layers 3 and 5, respectively. Layer 3 diopsides have higher TiO_2 and Al_2O_3 contents (0.17 to 3.07 wt.% TiO_2 and 3.57 to 10.8 wt.% Al_2O_3) than diopsides in layer 5 (<0.02 to 0.12 TiO_2 wt.% and 0.57 to 3.65 wt.% Al_2O_3). For diopsides of layer 3, there is a linear positive correlation between TiO_2 and Al_2O_3. In contrast, no such correlation was found for diopsides of layer 5. These differences indicate the lack of any crystal/liquid fractionation processes and strongly suggest that these layers did not form by crystallization from a common melt. In contrast to diopsides in the sinuous fragments, those in layers 3 and 5 have low V_2O_3, Cr_2O_3, MnO, and FeO contents (0.01 to 0.14 and <0.04 wt.% V_2O_3, respectively; <0.03 and <0.08 wt.% Cr_2O_3 and MnO; 0.02 to 0.53 wt.% in layer 3 and 0.03 to 0.81 wt.% FeO in layer 5). Examples of analyses of diopsides in both layers are shown in Table 8.

Olivine (layers 4 and 6). Sixty analyses were obtained on olivines of both layers and the olivine clumps (Fig. 10b). Only grains > 10 µm were analyzed to avoid the contribution of minor elements (e.g., CaO) because of contamination from neighboring diopsides. Olivines of layer 4 display a narrower compositional range ($Fo_{96.3}$ to Fo_{99}) than olivines in layer 6 (Fo_{93} to Fo_{99}). Olivines from both layers contain minor concentrations of Al_2O_3 (<0.01 to 0.81 wt.% in layer 4 and 0.01 to 0.45 wt.% in layer 6; Table 8). Grains in layer 4 contain more
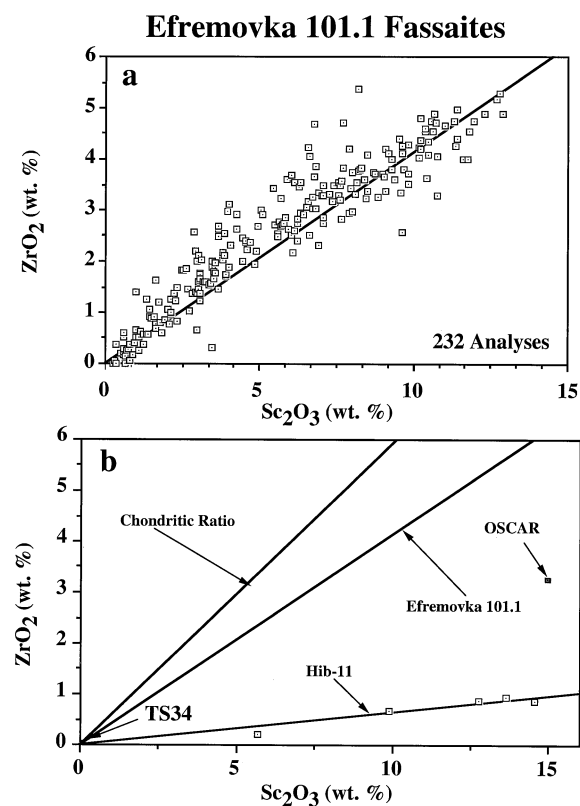
Efremovka 101.1 Fassaites

Fig. 15. (a) ZrO_2 vs. Sc_2O_3 contents of fassaites. Notice the good linear positive correlation between these oxides. (b) Comparison of the ZrO_2/Sc_2O_3 ratios in fassaites from Efremovka 101.1, OSCAR, Murch-11, TS34, and the chondritic ratio. Notice that none of the fassaites in these samples has a chondritic ratio. The correlation line for fassaites in Efremovka 101.1 is closest to the chondritic ratio line.

CaO than those in layer 6 (0.38 to 2.86 wt.% vs. 0.16 to 0.44 wt.%). The total number of cations of grains in both layers does not deviate from the olivine stoichiometry and thus indicates that the analyses were not contaminated from neighboring phases (columns 7 to 10 in Table 8).

3.4. Trace Elements

Several grains of each mineral species (except spinel) were analyzed. The obtained patterns are depicted in Figures 17 to 21. All minerals exhibit the same basic UR REE pattern but with distinct variations in the REE concentrations among different minerals.

3.4.1. Melilite

Patterns of four melilites in the host CAI and one from subinclusion 1 are shown in Figure 17. All melilites display UR REE patterns with enrichment factors of 2.5 to 8 relative to CI for La to Sm and 10 to 20 for Gd to Er and Lu. They also show substantial Eu excesses and Tm and Yb depletions as well as large Nb and V depletions. All melilites have higher La than Ce concentrations. This may have resulted from preferential enrichment of La relative to Ce in the liquid during crystallization

of fassaite before the onset of melilite crystallization. All melilites have much lower Sc and Zr than Y abundances.

3.4.2. Perovskite

Fourteen perovskite grains from the host CAI (A to C, E, and I to N), subinclusion 1 (D), and interiors of symplectitic refractory fragments (F to H in Fig. 8) were analyzed (Fig. 18). Hf was analyzed in perovskites F to N only. A wide rim of Sc- and Zr-rich fassaite (fassaite F in Fig. 19) around perovskite E was also analyzed, allowing a direct comparison between the elemental abundances of coexisting perovskite and the fassaite reaction rim.

Perovskites display UR patterns with enormous enrichments in the UR HREEs Gd to Er and Lu (800 to 5000 × CI) and large depletions in Eu and depletions in Tm and Yb. Erbium and Lu have, with few exceptions (E to G and J), comparable normalized abundances. The slope from Gd to Er varies among grains; some show a steep slope (C to E, K, and L), while others display a more gentle increase (F), accompanied by a lower abundance of Lu than of Er. Abundances for the LREEs (La to Sm) range from 300 to 1800 × CI. Inspection of the CI-normalized Tm-vs.-Er relationship in all analyzed perovskites revealed an excellent linear correlation with a positive slope of 0.37, thus indicating that the REE patterns of the various perovskites were produced with the same degree of volatility fractionation of these two elements. A similar linear correlation with a positive slope of 1.5 was also found between the CI-normalized Gd and Sm abundances. Neither the Tm/Er nor the Gd/Sm ratio varies with any other CI normalized ratio (e.g., Y/Zr). There are differences in the relative abundances of Zr, Y, Sc, Nb, and V among different grains. The ion probe measurements confirm the existence of the group 2 (B and C) and group 3 (D to G, I to N) perovskites defined on the basis of electron probe analyses. Members of group 4 (Fig. 13) were not measured by SIMS because these grains were too small (<10 μm) and could not be cleanly analyzed in the ion microprobe without contamination from their fassaite rims. We found also a grain with lower than chondritic Y/Zr ratio (group 1; Per A). Perovskite grains A and L have relatively higher Sc abundances (700 to 900 × CI) than the abundance of this element in other perovskites (8 to 200 × CI). The relative abundances of Zr, Y, and Sc are, with the exception of perovskite A, complementary to the abundances of these elements in Sc- and Zr-rich fassaites in the CAI core (Fig. 19). Niobium is more abundant in perovskites F to N (400 to 800 × CI) than perovskites A to D (100 to 400 × CI). Vanadium is depleted (11 to 100 × CI) in all but perovskites L and M (400 to 800 × CI).

3.4.3. Sc- and Zr-Rich Fassaite

The trace element patterns of eight fassaites are shown in Figure 19. We included in this figure also the pattern of fassaite C (layer 2 in the rim sequence) for comparison. Fassaites A and D to H are from the core of the CAI, and fassaite B is from subinclusion 1. Some of these fassaites (D and E) were selected close to or adjacent to the rim sequence to see whether these fassaites have similar patterns to those in the core or in the rim and if their patterns were overprinted or modified during the

EFREMOVKA 101.1 FASSAITES

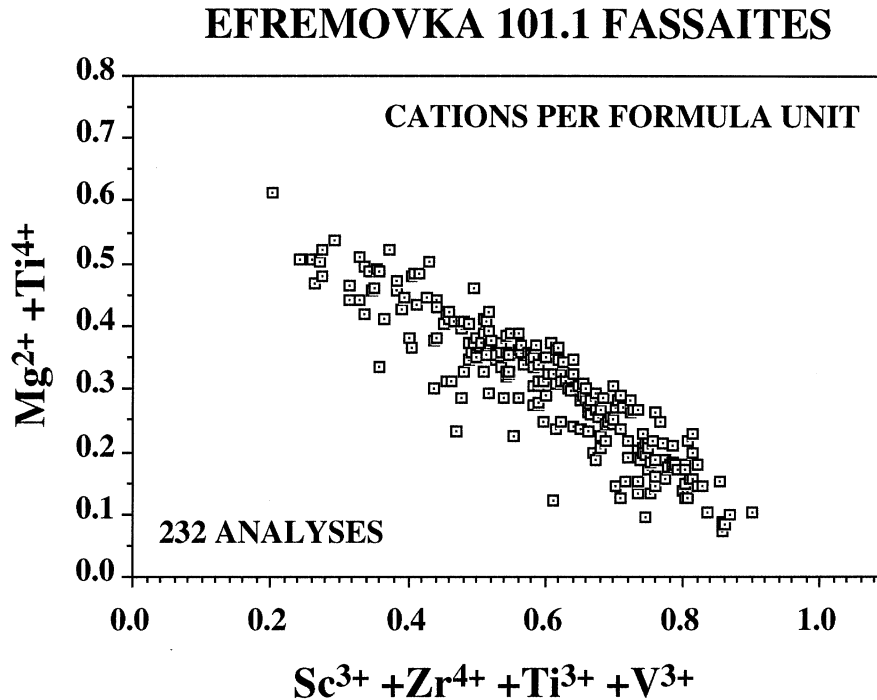**CATIONS PER FORMULA UNIT**

232 ANALYSES

Fig. 16. A plot depicting the cation substitutional relationship in fassaite. The coupled substitution is demonstrated by the good correlation between $Mg^{2+} + Ti^{4+}$ and $Sc^{3+} + Zr^{4+} + Ti^{3+} + V^{3+}$.

process of rim sequence formation (see discussion on the rim sequence formation).

All fassaites display UR REE patterns (Fig. 19). In contrast to the perovskites, with one exception (fassaite F), fassaites have higher abundances of Lu (200 to 500 × CI) than of the UR HREEs Gd to Er (25 to 150 × CI). The slope from the LREEs and further from Gd to Lu is also distinctly steeper (30 × CI for Gd to 500 × CI for Lu in fassaite D) than in perovskites (Fig. 18). This slope is very similar to those reported for fassaites in CTA TS32 (Simon et al., 1992). This fractionation is the result of the general tendency of fassaite to better incorporate HREEs than LREEs and the opposite behavior of perovskite. However, the steep patterns in fassaite evidently reflect the UR pattern of the parental liquid, since the higher abundances of the heavier HREEs (Yb, Lu) over the lighter HREEs (Gd, Tb) cannot have resulted from fractionation of a late melt by melilite crystallization (Simon et al., 1991). In addition, all fassaites in 101.1 are enclosed in melilite cores, indicating formation before onset of melilite crystallization (see section 3.2). Only grains D to F from the CAI core and B from subinclusion 1 have Eu depletions. The pattern of grain F (rim around perovskite E) that has much higher LREE abundances than the others (and as a consequence a more pronounced Eu anomaly) might have been contaminated by some perovskite. However, the relatively low Y abundance argues against contamination due to a possible beam overlap on perovskite E core during analysis. The pattern of fassaite F presumably resulted from both crystal/liquid fractionation and subsolidus equilibration with perovskite E. Since Sc is compatible with the fassaite structure and La is not, a linear corre-

Table 6. Composition of diopside and Al-diopside layers in the rim sequence of subinclusion 1 (wt. % and cation number) as measured by electron microprobe.

Oxides	1	2	3	4
CaO	25.4	25.1	25.6	25.8
MgO	18.4	18.3	16.6	16.5
FeO	0.20	0.17	0.12	0.06
MnO	n.d.	n.d.	n.d.	0.01
TiO_2	n.d	n.d.	0.10	0.15
V_2O_3	n.d.	n.d.	0.04	n.d.
Cr_2O_3	0.04	0.03	0.09	0.06
Al_2O_3	0.24	0.41	5.25	5.03
SiO_2	56.1	56.4	52.0	52.4
Y_2O_3	n.d.	n.d.	n.d.	n.d.
Sc_2O_3	n.d.	n.d.	n.d.	n.d.
ZrO_2	n.d.	n.d.	n.d.	n.d.
Total	100.38	100.41	99.80	99.01
Number of cations per formula unit				
Ca	0.979	0.970	0.993	0.998
Mg	0.985	0.979	0.893	0.887
Fe	0.005	0.004	0.003	0.001
Mn	0.000	0.000	0.000	0.000
Ti	0.000	0.000	0.002	0.003
V	0.000	0.000	0.001	0.000
Cr	0.000	0.000	0.002	0.001
Al	0.009	0.017	0.223	0.214
Si	2.02	2.029	1.882	1.895
Y	0.000	0.000	0.000	0.000
Sc	0.000	0.000	0.000	0.000
Zr	0.000	0.000	0.000	0.000
Total	3.998	3.999	3.999	3.999

Analyses 1 and 2 diopside, 3 and 4 Al-diopside.
n.d. = not detected.

Table 7. Andradite and wollastonite compositions in the rim sequence of subinclusion 1 (wt. % and cation number) as measured by electron microprobe.

Oxides	Andradite[a]	Wollastonite[a]
CaO	28.5	39.1
FeO	27.8	1.57
MnO	0.16	0.03
MgO	5.14	3.03
TiO_2	0.01	0.02
Na_2O	0.03	0.22
Al_2O_3	0.57	4.36
SiO_2	30.5	45.9
Total	92.71	94.23
Number of cations per formula unit		
Ca	2.959	0.845
Fe	2.256	0.026
Mn	0.011	0.000
Mg	0.743	0.090
Ti	0.000	0.000
Na	0.002	0.008
Al	0.065	0.104
Si	2.959	0.926
Total	8.995	1.999

[a] Analyses with the best totals out of six andradites and four wollastonites.

lation is expected between these elements should their concentration in fassaite have solely resulted from crystal/liquid fractionation (Simon et al., 1991). A plot of these elements did not reveal any correlation. We explain this lack of correlation between Sc and La by invoking subsolidus fractionation of Sc (and perhaps La) between fassaite and perovskite that overprinted the original relationship.

The refractory lithofile trace element (RLTE) patterns also reveal important differences between core fassaites and rim fassaite C on one hand and core fassaites and perovskites on the other hand (Fig. 19). All fassaites have relatively low Ba (3 to 10 × CI) but high V (300 to 500 × CI) abundances. Except for rim fassaite C, the relative abundance patterns of Zr, Y, Sc, and Nb are complementary to those in perovskites (Fig. 18): depletions in Y and Nb relative to Zr and Sc. However, Y and Nb are still enriched relative to CI. This complementary relationship must have resulted from both crystal/liquid and solid/solid fractionation processes, with Zr and Sc preferring fassaite and Y and Nb perovskite (see also Simon et al., 1994). The REE pattern of fassaite C differs from those of the core fassaites, indicating that it was not produced by the same process. It displays a remarkable Eu depletion and has entirely different Zr and Sc abundances. Yttrium and Sc abundances are similar and Zr (315 × CI) is only slightly enriched over Y (120 × CI), in contrast to the sharp differences in all fassaites below the rim sequence (4000 × CI for Zr vs. 150 × CI for Y). More will be said about this in the discussion on trace elements and on rim sequence formation.

3.4.4. Diopside

The trace element abundances of two diopsides from sinuous fragments (diopsides A and B from fragments S7 and S8) and

Table 8. Compositions of Sc-fassaite (layer 2), Al-diopside and diopside (layers 3 and 5), and olivine (layers 4 and 6) as measured by electron microprobe in the rim sequence of 101.1.

Oxide	1	2	3	4	5	6	7	8	9	10
CaO	22.3	24.6	25.4	25.1	25.9	26.2	0.38	2.86	0.16	0.44
MgO	6.6	11.2	16.3	14.4	17.9	16.0	56.1	52.8	55.8	54.3
FeO	0.72	0.62	0.06	0.03	0.10	0.06	1.41	1.43	2.61	2.03
MnO	n.d.	0.02	n.d.	n.d.	n.d.	n.d.	0.05	0.02	0.03	n.d.
TiO_2	12.3	3.51	0.17	3.07	n.d.	0.05	<0.02	0.12	<0.01	n.d.
V_2O_3	0.82	0.18	<0.01	0.11	n.d.	n.d.	n.d.	0.03	n.d.	n.d.
Cr_2O_3	0.07	0.08	0.09	0.07	0.09	0.08	0.04	0.05	0.07	0.07
Al_2O_3	24.5	13.4	4.36	10.8	2.39	3.7	0.09	0.81	0.19	0.45
SiO_2	31.2	45.2	52.1	47.8	53.6	53.1	40.9	43.0	42.3	41.7
Na_2O	<0.02	<0.01	n.d.	n.d.	n.d.	n.d.	<0.01	n.d.	n.d.	<0.01
Sc_2O_3	0.77	0.08	n.d.	0.06	n.d.	n.d.	n.d.	n.d.	n.d.	n.d.
Total	99.10	98.89	98.48	101.4	99.98	99.19	98.97	101.1	101.5	98.99
Number of cations per formula unit										
Ca	0.943	0.980	0.996	0.958	1.003	1.021	0.009	0.072	0.003	0.01
Mg	0.369	0.622	0.887	0.766	0.962	0.867	1.987	1.859	1.948	1.938
Fe	0.022	0.019	0.001	0.000	0.002	0.001	0.026	0.027	0.051	0.04
Mn	0.000	0.000	0.000	0.000	0.000	0.000	0.000	0.000	0.000	0.000
Ti^{4+}	0.160	0.000	0.004	0.082	0.000	0.001	0.000	0.002	0.000	0.000
Ti^{3+}	0.189	0.097	0.000	0.000	0.000	0.000	0.000	0.000	0.000	0.000
V	0.024	0.005	0.000	0.003	0.000	0.000	0.000	0.000	0.000	0.000
Cr	0.001	0.002	0.002	0.001	0.002	0.002	0.000	0.000	0.000	0.001
Al	1.088	0.588	0.186	0.455	0.102	0.156	0.002	0.022	0.004	0.012
Si	1.178	1.683	1.908	1.708	1.936	1.933	0.972	1.016	0.991	0.998
Na	0.001	0.000	0.000	0.000	0.000	0.000	0.000	0.000	0.000	0.000
Sc	0.024	0.002	0.000	0.001	0.000	0.000	0.000	0.000	0.000	0.000
Total	3.999	3.998	3.986	3.974	4.007	3.981	2.998	2.998	2.997	2.998

Analyses 1 and 2 are from layer 2 fassaite, 3 and 4 are from layer 3 Al-diopside, 5 and 6 are from layer 5 diopside, 7 and 8 are from layer 4 olivine, and 9 and 10 are from layer 6 olivine.
n.d. = not detected.
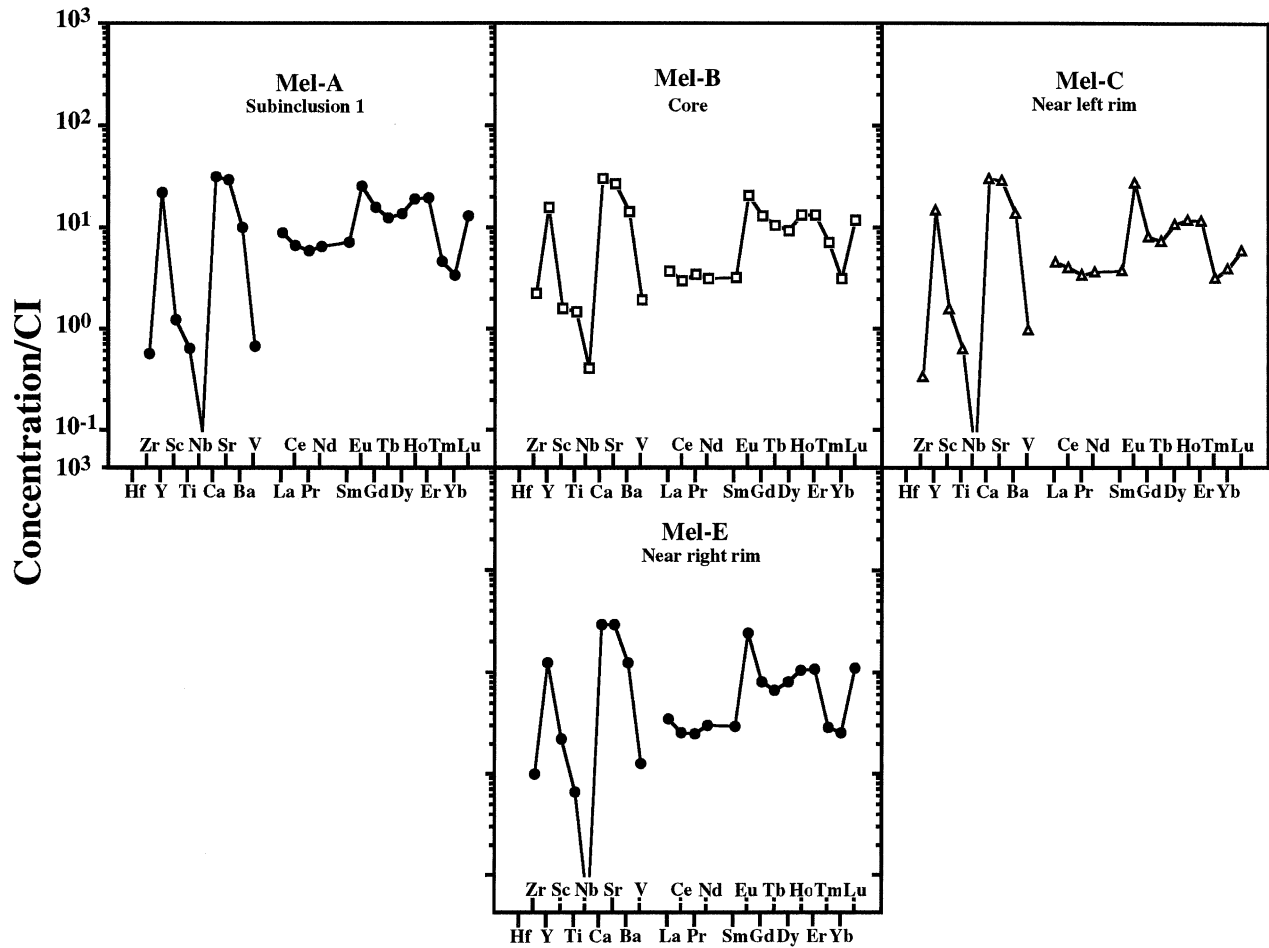
Efremovka 101.1

Fig. 17. Rare earth element and refractory lithophile element abundances in melilites from subinclusion 1 and the host Ca-Al-rich inclusion.

D from layer 5 of the rim sequence are shown in Figure 20. All three diopsides display a UR signature; however, the abundances are clearly lower than those of fassaites. Diopside B shows a positive Eu anomaly that is perhaps an artifact because of ion beam overlap onto the neighboring core melilite. However, the pattern is compatible with those of the other diopsides, indicating minor contamination. All three diopsides have a steep slope from Gd to Sm, but diopside D has higher REE abundances and Eu depletion. We observe also differences in the abundances of the RLTEs between the diopsides from the sinuous fragments and rim diopside D, and between diopsides of both types and the fassaites in the core. Diopside D is depleted in Ba ($0.6 \times$ CI) and enriched in V ($20 \times$ CI) in comparison to diopsides A and B (Ba 1.5 to $1.9 \times$ CI, V $2.0 \times$ CI). Its pattern is similar to that of fassaite C (Fig. 19). The relative abundances of Zr, Y, and Sc in all three diopsides are distinct from those of the core fassaites (Fig. 19). They show either equal abundances for Zr and Y and lower ones for Sc (diopside A), or higher Y than Zr and Sc abundances (diopside B). The pattern of these three elements in diopside D is the same as that in diopside A from the sinuous fragment, suggesting a similar process of formation.

3.4.5. Rim Sequence

The patterns of fassaite C (layer 2), diopside C (layer 3), diopside D (layer 5), and olivine A (layer 6) are given in Figure 21. Because of its small grain size and the danger of contamination from the neighboring diopside layers, olivine in layer 4 was not analyzed. The REE patterns of all layers analyzed show UR signatures with a steep rise from Gd to Lu. Analysis of diopside C was possibly contaminated by beam overlap onto neighboring or underlying Sc-fassaite (layer 2). However, the difference in the relative abundances of Y and Sc in fassaite C and diopside C indicates that the RLTE abundances measured were mainly intrinsic to the individual phases. There is a successive decrease in the REE abundances from layer 3 to layer 6, but with no dramatic change in the pattern of the HREEs. Layers 2, 3, and 5 have Eu depletions whose magnitudes decrease outward. All layers show slightly higher Ce than La abundances. This excess is most pronounced in the olivine from layer 6, which also has a Pr excess relative to La and Nd. It is remarkable that forsterite in layer 6 and in the clumps attached to the CAI rim sequence displays the same UR REE pattern as all other minerals.
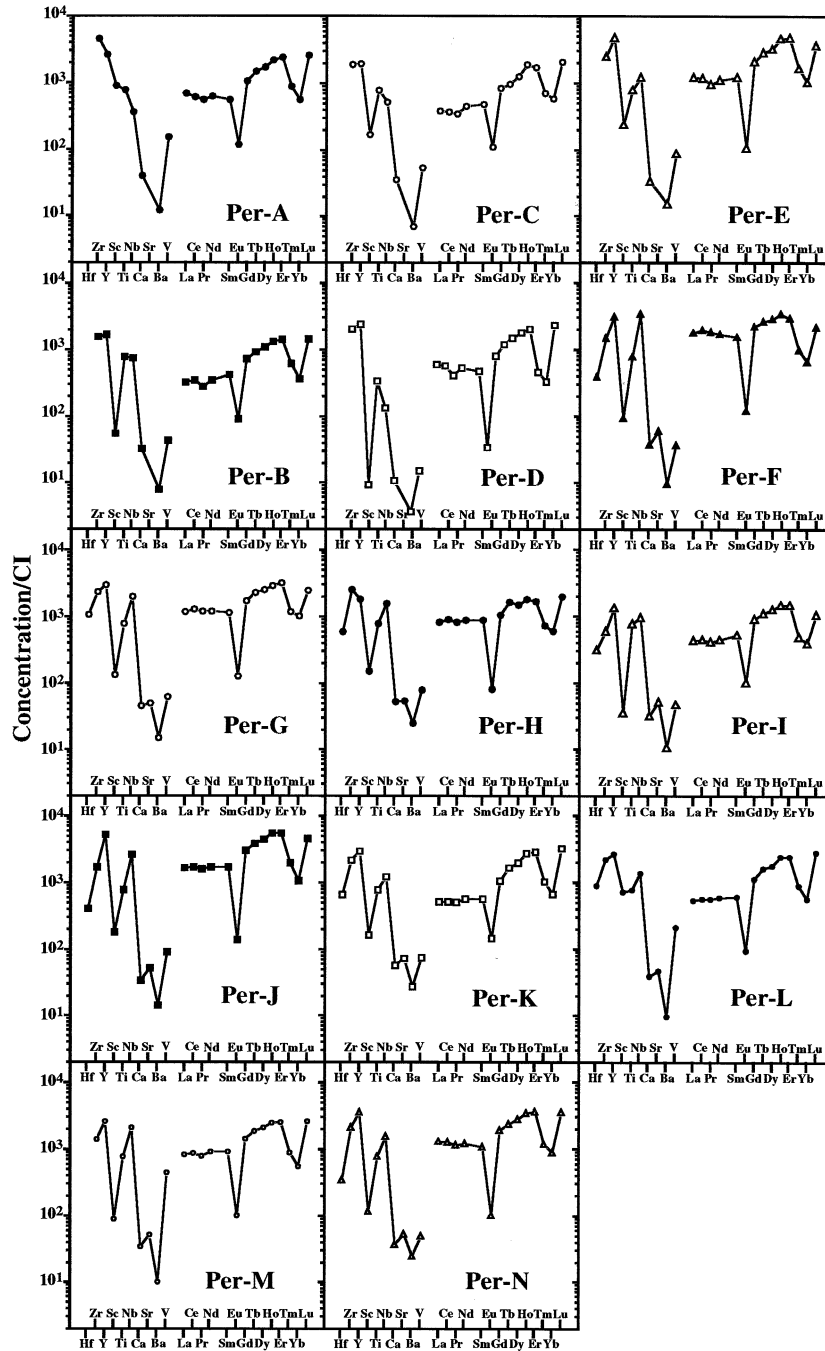
Fig. 18. Rare earth element and refractory lithophile element abundance patterns of 14 perovskites in the host Ca-Al-rich inclusion (A to C, E, I to N), subinclusion 1 (D), and in spinel-perovskite-fassaite fragments (F to H). See also Figure 8.

All layers are relatively enriched in V and depleted in Ba. Systematic changes in the abundances of the RLTE from layer 2 to layer 6 include not only a general decrease of abundances but also changes in the patterns. Fassaite C from layer 2 has similar Y and Sc but higher Zr abundances. Diopside C from the third layer has even higher Zr and a larger drop to Y and Sc. In contrast, the diopside D in layer 5 has equal Zr and Y abundances and a relative depletion in Sc. Olivine A in layer 6 has lower Zr than Y abundances and even lowers Sc.

3.5. Isotopic Compositions

3.5.1. Ca- and Ti-Isotopic Compositions

Three perovskites, I, B, and A, belonging to the three Y/Zr groups 1, 2, and 3, respectively (Figs. 13 and 18) were analyzed for their Ca and Ti isotopic compositions. Perovskite A is located in the core of the CAI, perovskite B is associated with a spinel cluster in the core (Fig. 4), and perovskite I is located
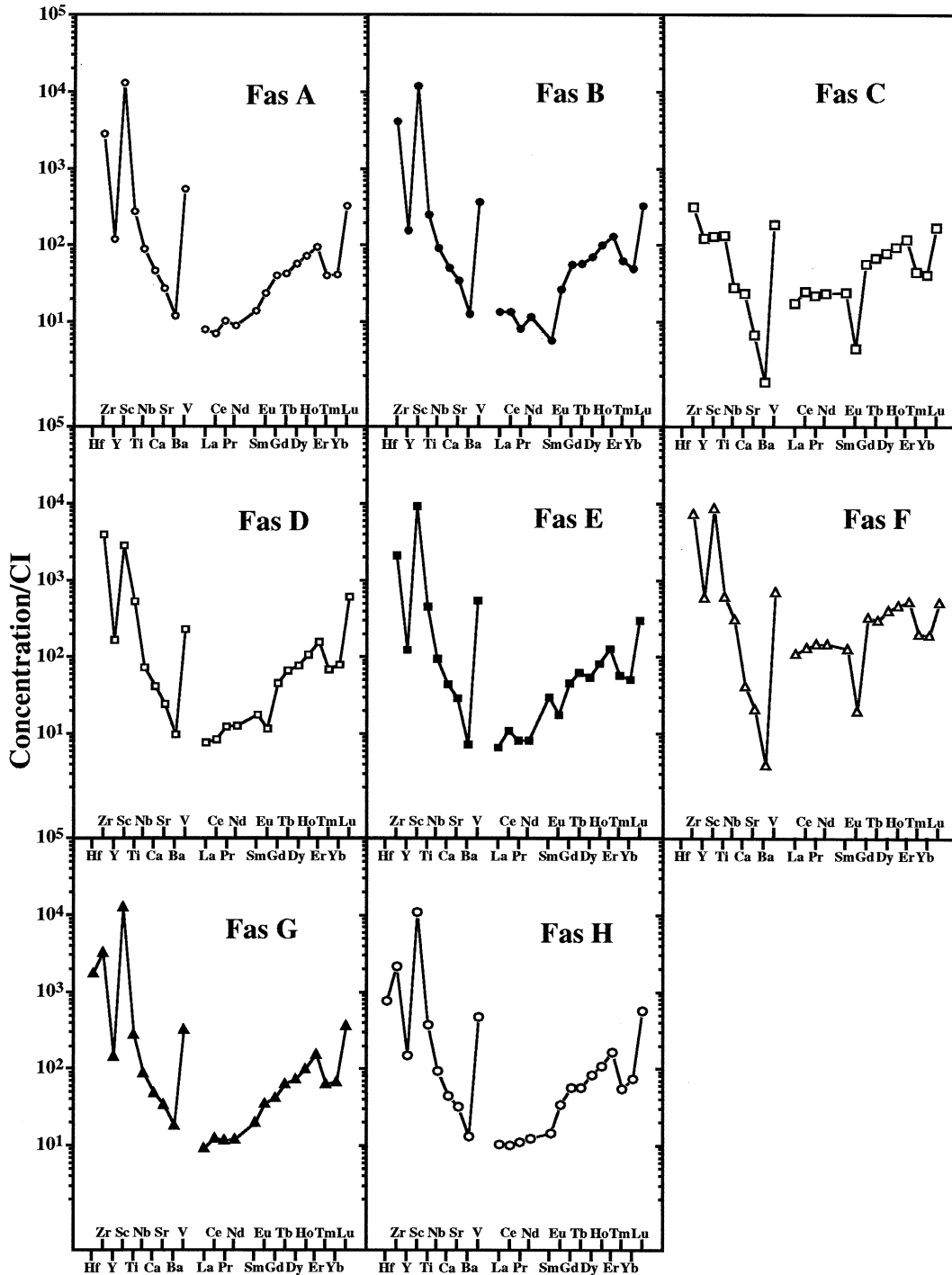
Fig. 19. Rare earth element and refractory lithophile element patterns of eight fassaites. Patterns A and D to H are from the core of the host Ca-Al-rich inclusion, B is from the core of subinclusion 1 (see Fig. 6a), and C is from layer 2 in the rim sequence. The relative abundances of Zr, Y, and Sc in fassaite C are distinct from those of all other fassaites measured in the host and subinclusion 1.

in the core of a fragment with symplectitic spinel-perovskite-fassaite intergrowth. Their Ca- and Ti-isotopic compositions are shown in Figure 22. Both perovskites A and I show well-resolved excesses in ^{48}Ca of δ^{48}Ca $= 9.8 \pm 2.1$ (1σ) and 4.5 $\pm$ 1.9‰, respectively, while perovskite B shows a deficit in this

isotope (δ^{48}Ca $= -7.5 \pm 2.7$‰). The Ti-isotopic compositions of all three perovskites are essentially normal. All three perovskites plot within the field of SHIB hibonites in a δ^{48}Ca-vs.-δ^{50}Ti plot (Ireland et al., 1988; Ireland, 1990; see Fig. 3 in Ireland et al., 1991). Apart from differences in their Ca-isotopic
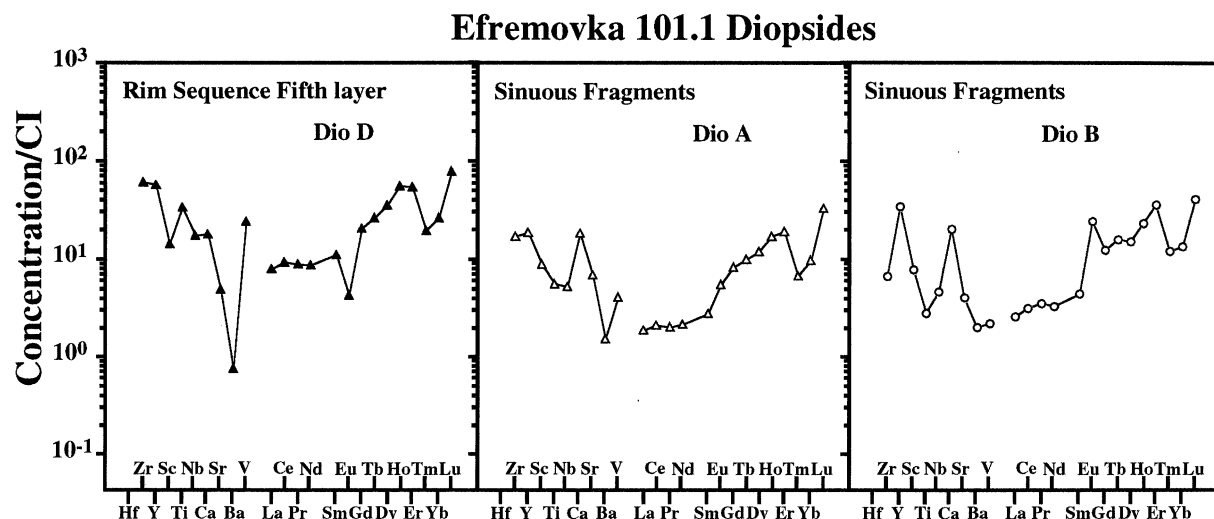
Efremovka 101.1 Diopsides

Fig. 20. Rare earth element and refractory lithophile element patterns of two diopsides from sinuous fragments 7 and 8 (A and B in Fig. 5b) and one diopside from layer 5 in the rim sequence of the host Ca-Al-rich inclusion (D).

compositions, these perovskites have different Y/Zr ratios, indicating that they did not form from the same refractory liquid but must have formed by different reservoirs.

3.5.2. Mg-Al Isotope Systematics

Results of the Mg-Al analyses are given in Table 9. We measured the intrinsic Mg isotopic mass fractionation to determine whether the UR REE signatures characteristic of all constituents of 101.1 were produced by evaporation. Three anorthites, 10 melilites, 3 diopsides (including diopsides from the rim sequence of subinclusion 1), and 7 spinels were analyzed. The locations and the petrographic units to which each grain belongs are given in Table 9.

Melilites in subinclusion 1 (analyses 1 to 4; Fig. 23) have clear ^{26}Mg excesses, with the data points defining a line with a slope of 4.3×10^{-5}. One analysis of a melilite in subinclusion 2 plots slightly above this line. Analyses of five melilites from the host CAI (analyses 5 to 9; Fig. 23) give variable ^{26}Mg excesses, with data points scattered above and below the slope 4.3×10^{-5} line of subinclusion 1. Anorthites in the sinuous fragments 7 and 8 and in the rim sequence of subinclusion 1 have no or only small (relative to their ^{27}Al/^{24}Mg ratios) ^{26}Mg excesses (Fig. 24). The data show that the Mg-Al system in the host CAI, the sinuous fragments, and in anorthite in the rim sequence of subinclusion 1, which are adjacent to the melt pockets, is disturbed due to partial isotopic equilibration of Mg during or after ^{26}Al decay, presumably during the impact event that caused local melting. The maximum slope obtained by connecting individual anorthite data points to the essentially normal Mg measured in diopside, 1.85×10^{-5} (Fig. 24), is much lower than the slope of 4.3×10^{-5} obtained in subinclusion 1 and the ratios inferred from the melilite data points in the host CAI. Evidently, the disturbance in the Al-Mg system affected the anorthites of the sinuous fragments the most and the melilites in subinclusions 1 and 2 the least. The sinuous fragments 7, 8, and 3 are close to an impact melt pocket. It is hence possible that the disturbance of the Al-Mg system is

related to the shock event that created the melt pockets in the CAI.

There are differences in the Mg isotopic mass fractionation among minerals in the host CAI, the captured sinuous fragments, and the subinclusions. While melilites and spinels in the host CAI are isotopically slightly heavy, minerals in the sinuous fragments and near the rim sequence are light (Table 9).

4. DISCUSSION

The bulk composition of inclusion 101.1, the textural relationships of the various lithologic units, the major and minor elemental compositions of the minerals, the REE and RLTE abundances of the bulk inclusion and of individual mineral grains, and the isotopic record indicate a complex formation history for inclusion 101.1. The evolutionary stages of the CAI include (a) accretion of solid condensates, from a gas with a superrefractory REE and RLTE pattern; (b) a short partial melting event; (c) incorporation of oxidized sinuous fragments, small CAIs, and CAI fragments in the reduced refractory liquid of the CAI; (d) solidification of the core and formation of the rim layers; and (e) incorporation into the Efremovka parent body, followed by an impact event that created the melt pockets in the host CAI and possibly disturbed the Al-Mg system in some parts of the CAI.

4.1. Significance of Bulk Composition

As mentioned earlier, the pattern of RLTEs in bulk inclusion 101.1 was calculated from the INAA data of inclusions 101.1 + 101.2 and the SIMS data of 101.2. The resulting 101.1 pattern displays a comparatively smooth decline in element abundances with increasing volatility (Fig. 2). Such UR patterns are rare. They were found in very small inclusions of the Ornans and Murchison meteorites (see introduction), but never in the relatively large coarse-grained inclusions from CV-meteorites. Figure 2 clearly demonstrates the complementary relationship between 101.2 with a Group II pattern and 101.1
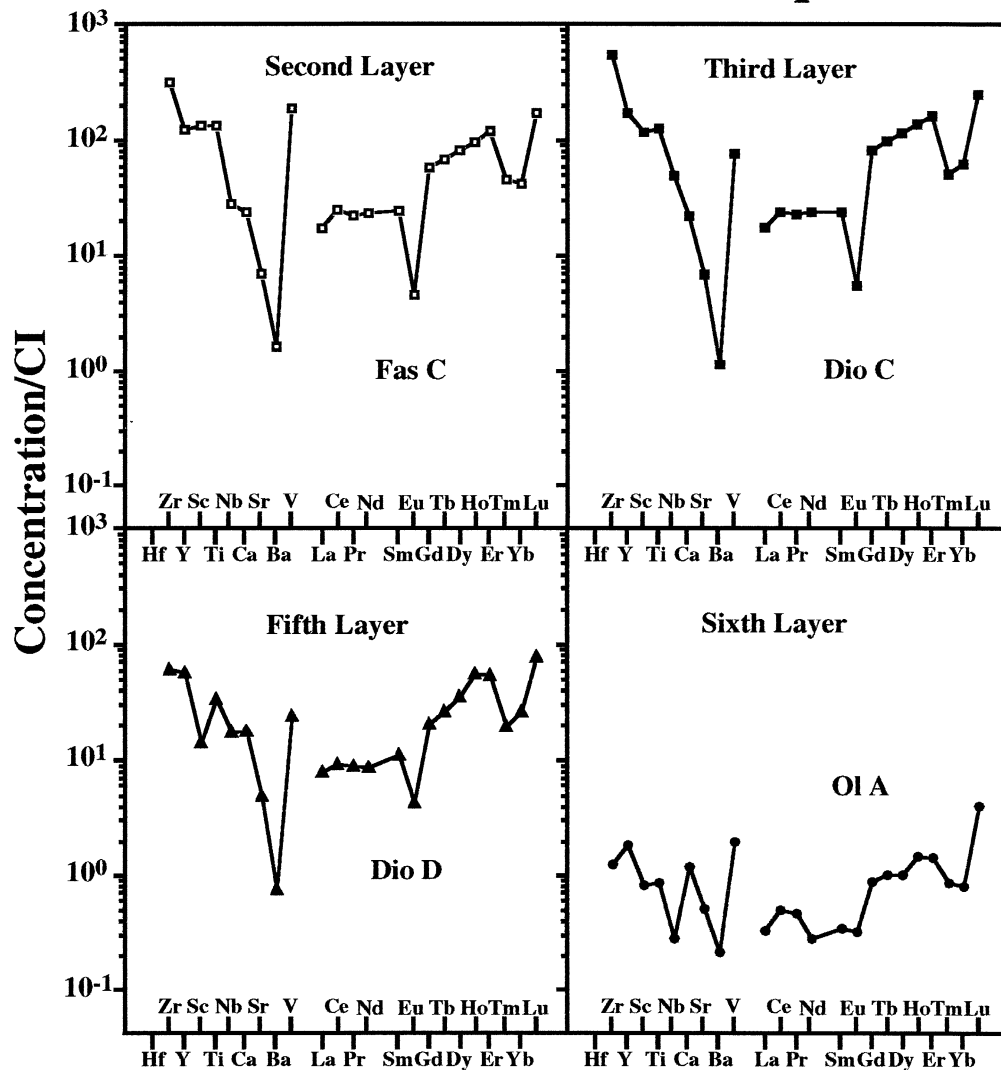
Efremovka 101.1 Rim Sequence

Fig. 21. Rare earth element (REE) and refractory lithophile element (RLE) patterns for fassaite C (layer 2), diopside C (layer 3), diopside D (layer 5), and olivine A (layer 6) from the host rim sequence. The RLE patterns of fassaite and diopside are different from those of the fassaites in the core of the host (D and E in Fig. 19). Although REE and refractory lithophile trace element abundances decrease from layer 2 to layer 6, the basic ultrarefractory pattern is observed in all rim layers.

with a UR pattern. The combination of both patterns yields the relatively flat pattern obtained for the bulk sample containing both inclusions. The complementary relationship is particularly important for elements between Tb and Yb (Fig. 2). From Figures 17 to 21, it is apparent that all individual phases in 101.1 have higher than chondritic Lu/La ratios, while 101.2 has a lower ratio, and the bulk sample has the chondritic ratio (Fig. 2). The spatial proximity of 101.1 and 101.2 and their complementary relationship suggest that both inclusions formed from the same small reservoir (or source) with essentially chondritic composition. The condensation of 101.1 may have depleted the gaseous reservoir in UR elements, thus leading to the Group II pattern of 101.2 during subsequent condensation.

4.2. RLEs in Coexisting Minerals

The more or less continuous decrease in abundances with decreasing condensation temperatures in 101.1 (Fig. 1) is also apparent from the ion probe data for individual minerals. Averages for perovskite, fassaite, and melilite (see Table 9) are shown in Figure 25. The smooth decrease in abundances with increasing volatility in all minerals is indicative of the prevailing UR trace element pattern. Some discontinuities in the patterns may reflect local mineral-melt or mineral-mineral equilibria. The low contents of Zr, Sc, and Nb in melilite, for example, is characteristic of this mineral; also, the high Zr and Sc in fassaite and the low Sc in perovskite may have been
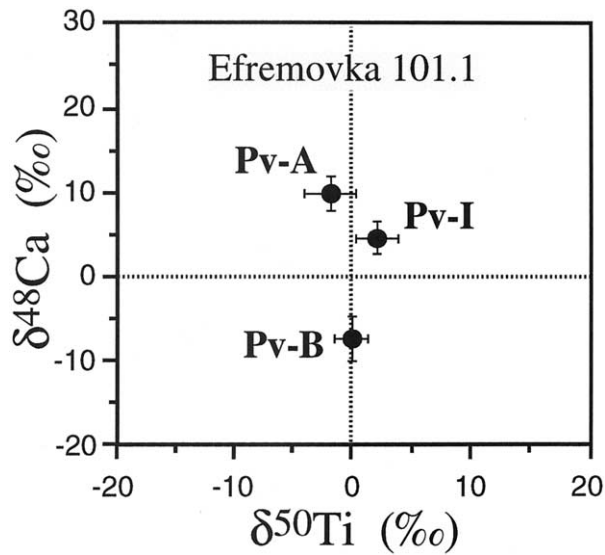
Fig. 22. Ca- and Ti-isotopic compositions of perovskites A, B, and I (Y/Zr groups 3, 2, and 1, respectively; see Figs. 4, 6a, 8, 13, and 18). Perovskites A and I show excesses in [48]Ca, while B has a deficit. The [50]Ti/[48]Ti ratio of the three grains does not deviate from normal.

Table 9. Mg isotopic ratios and Al/Mg ratios in individual minerals.

Al/Mg ± 1σ	F_{Mg} (‰/amu) ±1σ	[26]Mg/[24]Mg ±1σ
Subinclusion 1		
Spinel		
2.90 ± 0.03	1.4 ± 0.9	0.13953 ± 0.00018
3.00 ± 0.03	1.2 ± 0.8	0.13952 ± 0.00018
Melilite		
19.42 ± 0.03	−1.6 ± 1.2	0.14010 ± 0.00024
9.67 ± 0.01	0.0 ± 1.1	0.13988 ± 0.00017
16.84 ± 0.03	2.6 ± 1.1	0.14015 ± 0.00018
11.59 ± 0.03	1.0 ± 1.2	0.13995 ± 0.00019
Subinclusion 2		
Spinel		
2.84 ± 0.03	−1.7 ± 0.8	0.13968 ± 0.00019
Melilite		
16.63 ± 0.30	−1.9 ± 1.2	0.14051 ± 0.00025
Host inclusion		
Spinel		
2.758 ± 0.028	6.0 ± 0.8	0.13961 ± 0.00008
2.824 ± 0.022	5.7 ± 0.7	0.13932 ± 0.00016
2.243 ± 0.008	3.8 ± 0.9	0.13964 ± 0.00014
2.849 ± 0.029	3.0 ± 1.0	0.13944 ± 0.00018
2.979 ± 0.025	3.7 ± 0.8	0.13938 ± 0.00015
Melilite		
10.07 ± 0.59	2.5 ± 0.9	0.13966 ± 0.00012
13.33 ± 0.04	3.8 ± 1.1	0.14040 ± 0.00014
22.47 ± 0.40	5.7 ± 1.5	0.14047 ± 0.00026
13.65 ± 0.07	3.5 ± 1.1	0.13976 ± 0.00009
8.90 ± 0.07	3.4 ± 1.3	0.13976 ± 0.00009
Sinuous		
fragment		
Diopside		
0.19 ± 0.01	2.6 ± 1.0	0.13937 ± 0.00015
0.18 ± 0.01	1.9 ± 0.7	0.13940 ± 0.00015
Anorthite		
526 ± 4		0.14180 ± 0.00139
631 ± 26	−1.5 ± 7.6	0.13913 ± 0.00166
885 ± 5	−2.6 ± 6.2	0.13896 ± 0.00141
264 ± 15	−8.8 ± 4.1	0.14039 ± 0.00082
149 ± 4	−5.4 ± 3.8	0.14215 ± 0.00054

established by local exchange processes. The REE pattern in fassaite is, however, nearly identical to that of melilite. This is a clear reflection of the absence of equilibrium among the phases of the inclusion.

The low Zr and Sc in melilite and the complementary high contents in fassaite indicate limited exchange between melilite and fassaite. The apparent contradictory behavior of Sc and Zr (and Hf) on one hand and REEs on the other hand is also found in Allende CAIs (Palme et al., 1994). Very similar REE patterns were encountered in melilite and in fassaite mineral fragments of the Allende CAI Egg 6, but large variations and complementary relationships for Ti, Sc, and Hf.

Perovskite may be regarded as the only primary host phase of RLEs. A condensation origin for perovskite is very likely, considering the large variations of the Y/Zr ratio and the differences in Ca isotopic compositions (see below). Fassaite may have formed from initial perovskite through reaction with the CAI liquid and may have partly equilibrated with perovskite, leading to the enormous Sc and Zr concentrations in fassaite, even though equilibrium distribution of REEs was not achieved.

Condensation of melilite may initially have occurred on perovskite grains at a time when the REEs had been almost completely removed from the gas. Continuing condensation of melilite increasingly diluted the REEs but under retention of the original pattern. Limited exchange with fassaite and perovskite depleted melilite in Sc, Hf, Zr, and Nb, but because of lower mobility of the REEs, the REE pattern did not change during this process. Whatever the detailed history of 101.1, it must be emphasized that an origin by continuous evaporation is excluded. Heating and subsequent loss of the less refractory elements would have led to equilibration among mineral phases, would have destroyed the similarities in REE patterns

between perovskite, fassaite, and melilite and the different isotopic signatures of perovskites.

4.3. Significance of Relative Abundances of Y, Zr, and Sc in Perovskite and Fassaite

Simon et al. (1994) conducted a detailed experimental investigation on the partitioning of Zr, Y, and the REEs between perovskite and liquid. Their study indicates that the LREEs are highly compatible elements in perovskite, but the distribution coefficients (D) drop sharply for the HREEs, Y, and Zr. Igneous perovskite will then display uniform LREE (La to Sm) enrichment of the D pattern. An exception is perovskite found in igneous spinel-perovskite CAIs. Here, perovskite will display the whole-rock pattern, because spinel incorporates only a negligible fraction of the bulk REEs. In addition, Simon et al. (1994) concluded that it is difficult for Y and Zr to reach concentrations in perovskite above the chondritic values (i.e., concentrations corresponding to chondritic Y/Ti and Zr/Ti ratios) by crystal/liquid fractionation from a melt with uniform enrichment of refractory elements. Even more important is the experimental evidence that crystal/liquid fractionation from a
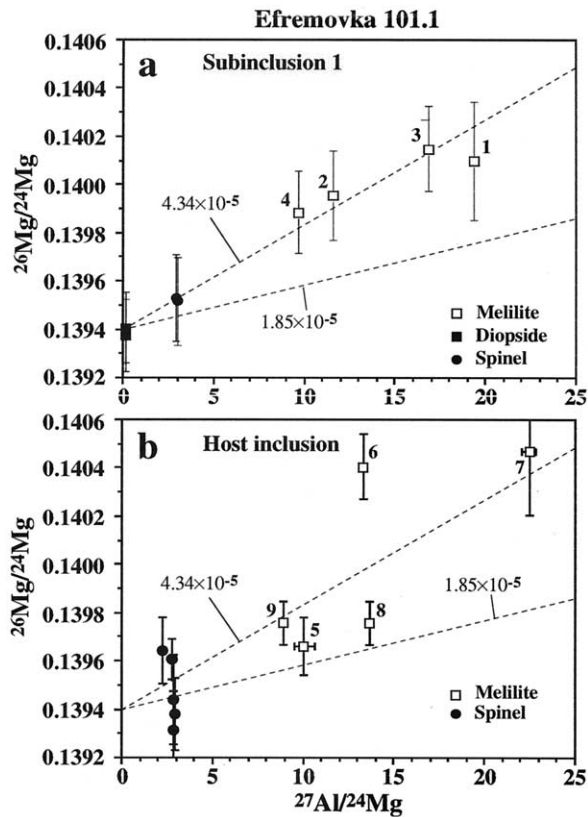
Fig. 23. Mg-Al isotopic systematics of melilite, diopside, and spinel in subinclusion 1 (Fig. 6a), and melilite and spinel from the host Ca-Al-rich inclusion.

liquid with chondritic Y/Zr ratio results in a higher than chondritic Y/Zr ratio in perovskite. The results of the experimental study by Simon et al. (1994) may be used to distinguish between an igneous origin (Y/Zr > CI ratio) and an origin by condensation (Y/Zr = CI ratio) or another nonigneous process. The Y/Zr ratios in perovskite thus present a diagnostic signature that allows one not only to identify perovskites crystallized from the CAI liquid but also to distinguish between various families of extraneous grains.

The presence of several perovskite populations with different Y_2O_3/ZrO_2 ratios (Fig. 13) indicates that not all perovskites formed by the same mechanism. Only a few (6 out of 76) have ratios that agree with the experimentally determined crystal/liquid fractionation ratio (Simon et al., 1994). About 21% of the perovskites have chondritic Y_2O_3/ZrO_2 ratios and are most likely direct condensates from a gas of solar composition. Yttrium could have condensed as Y_2O_3 in ZrO_2, which in turn was consumed by the later condensing perovskite (Kornacki and Fegley, 1986) without changing the original Y_2O_3/ZrO_2 ratio. Another alternative is that both oxides condensed (along with the other REE oxides) in hibonite, which in turn was consumed by the later condensing perovskite. However, it is very unlikely that hibonite was the primary host phase in 101.1 since (a) complete replacement of hibonite by perovskite would have then taken place without disturbing the Y_2O_3/ZrO_2 ratios and the Ca isotopic anomalies of every perovskite grain of the

same category, and (b) none of the perovskites in 101.1 contain any relics of hibonite. Whatever the origin of the chondritic Y_2O_3/ZrO_2 ratio in perovskite is (either in ZrO_2 or perovskite), this ratio is the fingerprint of the ratio in the gas from which either phase directly condensed. Perovskites of groups 1 and 4 and grains of group 3b must have formed by different mechanisms than group 1 and the six igneous perovskite grains. Their Y/Zr ratios could not have been produced by crystal/liquid fractionation from a CAI liquid with a solar Y/Zr ratio. Depletion of Zr in group 4 perovskites could be explained by the removal of the UR ZrO_2 condensates from the solar gas before the start of Y_2O_3 and perovskite condensation. In contrast, the depletion of group 1 perovskites in Y could not have been produced by a similar process for the following reason. Equilibrium condensation calculations of RLTEs at 10^{-3} bars total pressure from a gas of solar composition indicate that ZrO_2, HfO_2, Sc_2O_3, and Y_2O_3 condense as pure phases at 1786, 1753, 1724, and 1692 K, respectively, before the first appearance of perovskite at 1676 K (Kornacki and Fegley, 1986). It is hence difficult to selectively remove Y_2O_3 condensates just after condensation of ZrO_2, HfO_2, and Sc_2O_3 and before condensation of perovskite without depleting the UR dust in the four oxide condensates altogether. On the other hand, local subsolidus equilibration between perovskite cores and fassaite rims would rather lead to depletions of ZrO_2 and Sc_2O_3 and enrichment of Y_2O_3 in perovskites (see below).

It is conceivable that subsolidus diffusion of Zr from perovskite cores to their fassaite rims has contributed to the Y/Zr fractionation in perovskite. However, this fractionation could never have been the sole process leading to the formation of essentially Zr-free perovskite because one would then expect all perovskites with fassaite reaction rims to be Zr free. This is not the case. Equilibration between group 2 perovskites and the CAI liquid could also have shifted their Y/Zr ratios to higher values, thus producing group 3b perovskites. Since perovskites A (group 1), B (group 2), and I (group 3) show resolved differences in their Ca isotopic compositions, it is evident that they do not come from the same source and that the partial melting event in Efremovka 101.1 was so short that it did not erase their isotopic signatures.

Most Sc- and Zr-fassaites in 101.1 formed by reaction between the CAI liquid and preexisting perovskite and FeNi metal. They occur as rims around perovskite or FeNi metal. This occurrence and the contrasting zoning behavior of Sc_2O_3, ZrO_2, and V_2O_3 in these fassaites strongly support the proposed reaction. Partitioning of elements such as Zr, Y, Sc, and V between perovskite and fassaite very probably took place during subsolidus equilibration. To further explore the validity of this assumption, we compare the ZrO_2/Sc_2O_3 ratios in Sc-Zr-fassaites from Efremovka 101.1 with the chondritic ratio and with those in Sc-Zr-fassaites from OSCAR (Davis, 1984) and Hib-11 (Simon et al., 1996) in Figure 15b. It can be seen that none of the studied Sc-Zr-fassaites fall on the chondritic ratio line. Sc-Zr-fassaites in Hib-11 show the maximum deviation from the chondritic ratio. The Sc-Zr-fassaites in Efremovka 101.1 have close to chondritic ratios, while the OSCAR fassaite plots in between. The data points of Sc-Zr-fassaites in Hib-11 strongly suggest Zr/Sc fractionation. Simon et al. (1996) concluded that Hib-11 had solid condensate precursors that were melted and that spinel, perovskite, and Sc-Zr-fassaites formed
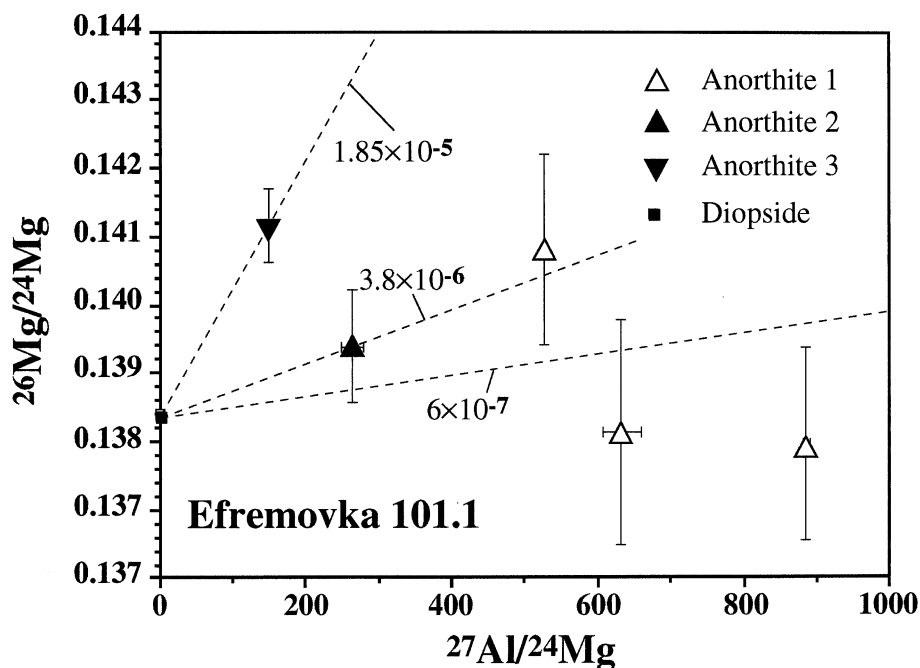
Fig. 24. Mg-Al isotopic systematics of anorthite and diopside from sinuous inclusions 7 and 8 (anorthites 1 and 2 and diopsides 1 and 2, respectively; (Fig. 5b), and anorthite 3 (rim sequence of subinclusion 1, Fig. 6a).

by crystallization from this melt. The smaller deviation of the ZrO_2/Sc_2O_3 ratios in Efremovka Sc-Zr-fassaites from the chondritic ratio in comparison to those in OSCAR and Hib-11 Sc-Zr-fassaites indicates a limited equilibration between the crystallizing Sc-Zr-fassaites and the Efremovka 101.1 melt, perhaps through shielding by the crystallizing melilite. Further partitioning of elements such as Zr, Y, Sc, and V between perovskite and fassaite very probably took place during subsolidus equilibration.

The slope of the correlation line between CI-normalized Zr and Sc in fassaites from 101.1 is 0.7, markedly different from the negative correlation reported for Type B CAIs by Simon et al. (1991). The Sc/Zr ratios in 101.1 have an average value of 0.99 in fassaites around FeNi metal and an average value of 1.52 in fassaites around perovskite. This clearly demonstrates the preference for Sc over Zr in fassaite during the subsolidus perovskite/fassaite equilibration. The absence of a correlation similar to that reported by Simon et al. (1991) must also have been due to the difference between the composition of the Efremovka host CAI liquid and that of Type B CAIs, resulting in a distinct crystallization sequence in the Efremovka inclusion.

4.4. Relict Grains

Considerable analytical and experimental efforts have been devoted to the search for relict perovskite, hibonite, and spinel grains in CAIs, as well as for desorbed perovskites in melilite in Type A and B CAIs. Johnson et al. (1988) reported excesses of lithophile trace elements in melilite in a Type B CAI that cannot be reconciled with the experimentally determined crystal/liquid D values (Beckett et al., 1990). They also found elevated Ti concentrations in cores of some melilites without

resolvable perovskite residues. These findings were interpreted as evidence for perovskite resorption in the refractory CAI liquid. In agreement with Johnson et al. (1988), Kennedy et al. (1991) reported that dissolution of heterogeneously distributed relict perovskite during melilite crystallization can explain both the localized melt enrichment in Ti and the REEs and the lack of any relationship between the åkermanite content and the trace element concentration in melilite. In fact, experimental investigations of the crystal/liquid trace element partitioning showed that the REEs and Th and U of many perovskites from Type B CAI are incompatible with an igneous origin (Kennedy et al., 1994; 1997). In situ isotopic analysis by SIMS techniques revealed the presence of isotopically anomalous perovskites and spinels in various types of CAIs. In a complex CAI from Efremovka, Goswami et al. (1991) reported ^{50}Ti excesses in some hibonite and perovskite grains, while other perovskites are isotopically normal. Relict spinels with isotopically heavier Mg than in the coexisting melilite and other spinels were also reported from Efremovka E40 (Goswami et al., 1994). Petrologic and isotopic studies of plagioclase-olivine inclusions (POIs) from the Allende, Adelaide, Leoville, and Vigarano chondrites (Sheng et al., 1991) revealed that spinels are the major carriers of isotopically fractionated Mg in six POIs. Both isotopically light and heavy Mg was found in coexisting spinels in the same POI, different from the coexisting silicates. No correlation between F_{Mg} and spinel chemistry was found.

Two problems accompanied the search for extraneous mineral grains in CAIs in chondritic meteorites: (a) CAIs may have sampled a variety of extraneous perovskites with different REE and RLE patterns so that the patterns measured in melilites with high Ti concentrations are probably averages of patterns of resorbed, genetically unrelated pervoskites; and (b) not all
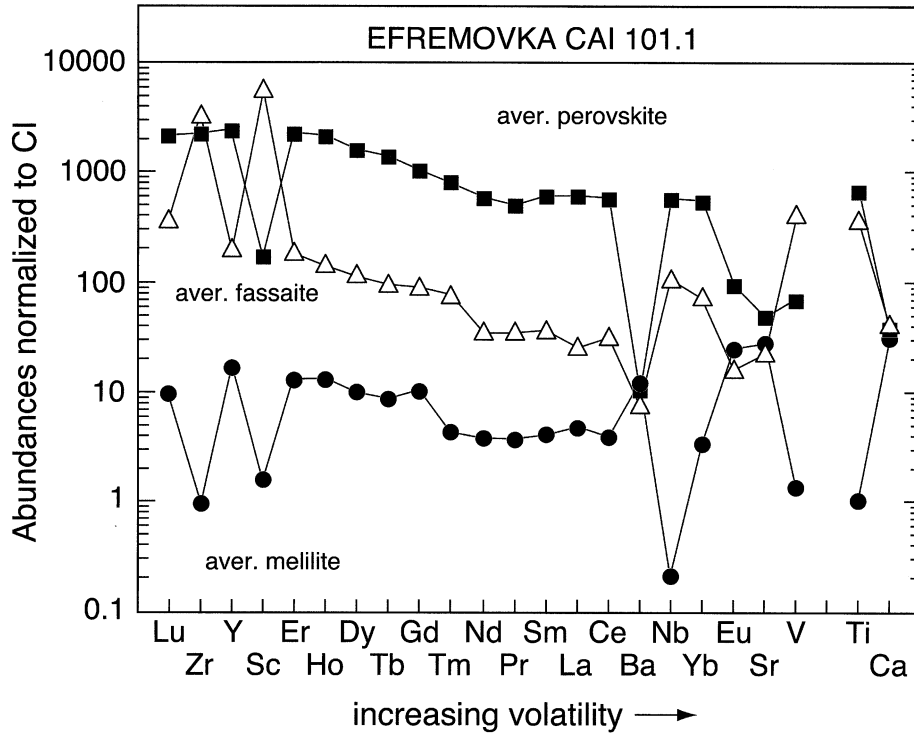
Fig. 25. Average normalized patterns of refractory lithophile trace elements (RLTEs) in various phases of 101.1. Elements are arranged according to increasing volatility. The rare earth element patterns are ultrarefractory and more or less parallel, reflecting lack of equilibrium among minerals. Other RLTEs appear to approach equilibrium distribution more closely: Zr, Sc, and Nb are low in melilite and high in fassaite (see text for details).

extraneous or relict hibonites, perovskites, and spinels are necessarily isotopically anomalous. Ion probe analysis will detect only the isotopically anomalous fraction of extraneous grains, while the isotopically normal (and perhaps the major fraction) will remain unrecognized. This approach will inevitably lead to a distorted picture about the inventory of extraneous grains in CAIs.

The sinuous fragments, many spinel clusters, most perovskites, and many FeNi metal blebs in Efremovka 101.1 apparently did not crystallize from the CAI liquid. The V_2O_3 and Cr_2O_3 contents of the spinels clearly resolve five distinct populations (Fig. 12a). Spinels in the rim sequence of the host CAI seem to be genetically unrelated to the other spinels. In addition, the limited, well-separated V_2O_3 and Cr_2O_3 concentration fields of several spinel populations in the host and subinclusions 1 and 2 indicate that they must have formed outside the host CAI. The spinels did not exchange minor elements such as V_2O_3, Cr_2O_3 and TiO_2 through subsolidus equilibration with their host melilites. Any subsolidus equilibration of the various spinel clusters with their host melilites would have erased the different V_2O_3, Cr_2O_3 and TiO_2 signatures and produced a uniform abundance of these oxides in the various clusters. The Mg isotopic composition of the spinels is normal, thus underlining our argument that the majority of these "isotopically normal" extraneous grains would be overlooked by the search for only isotopically anomalous grains. We argue that at least five different sources are required to explain the various spinel compositions. The positive V_2O_3-vs.-TiO_2 slope found in spinels from the outer regions of the first spinel cluster (Figs.

12a and 12b) in subinclusion 1 might have resulted from a sudden drop in f_{O_2} of the melt from which these spinels crystallized. Simon et al. (1992) reported a sharp rise in the V_2O_3 and TiO_2 contents in late-stage fassaites, which they attributed to a sudden drop in f_{O_2}. The decrease in f_{O_2} leads to an increase in the concentration of Ti^{3+} of the melt, resulting in partitioning of Ti^{3+} over Ti^{4+} in the late-stage fassaite. However, we caution that an analogy to late-stage fassaite cannot be drawn, because the spinels were the earliest phases in the refractory liquid, and it is not known if the preference for Ti^{3+} in spinel is similar to that in late-stage fassaite.

4.5. Possible Formational History of the Inclusion

A key to understanding the formation of 101.1 is, as discussed before, the striking similarity of the REE patterns in all phases of the inclusion. This suggests that all mineral species found in this CAI originated from the same reservoir with a UR REE signature. Incorporation of the sinuous fragments, the subinclusions, FeNi metals, spinel clusters, CAI fragments, and the majority of perovskites could have taken place either before or after partial melting. At any case, these fragments must have been incorporated before the formation of the rim sequence of the host CAI, since the rim layers entirely surround the host CAI (Fig. 3). We cannot exclude the possibility that the sinuous fragments are portions of a primordial rim sequence of the host CAI that was fragmented and pushed in the molten CAI droplet during the injection of the small subinclusions. Because oxidation and alteration assemblages are entirely confined to the
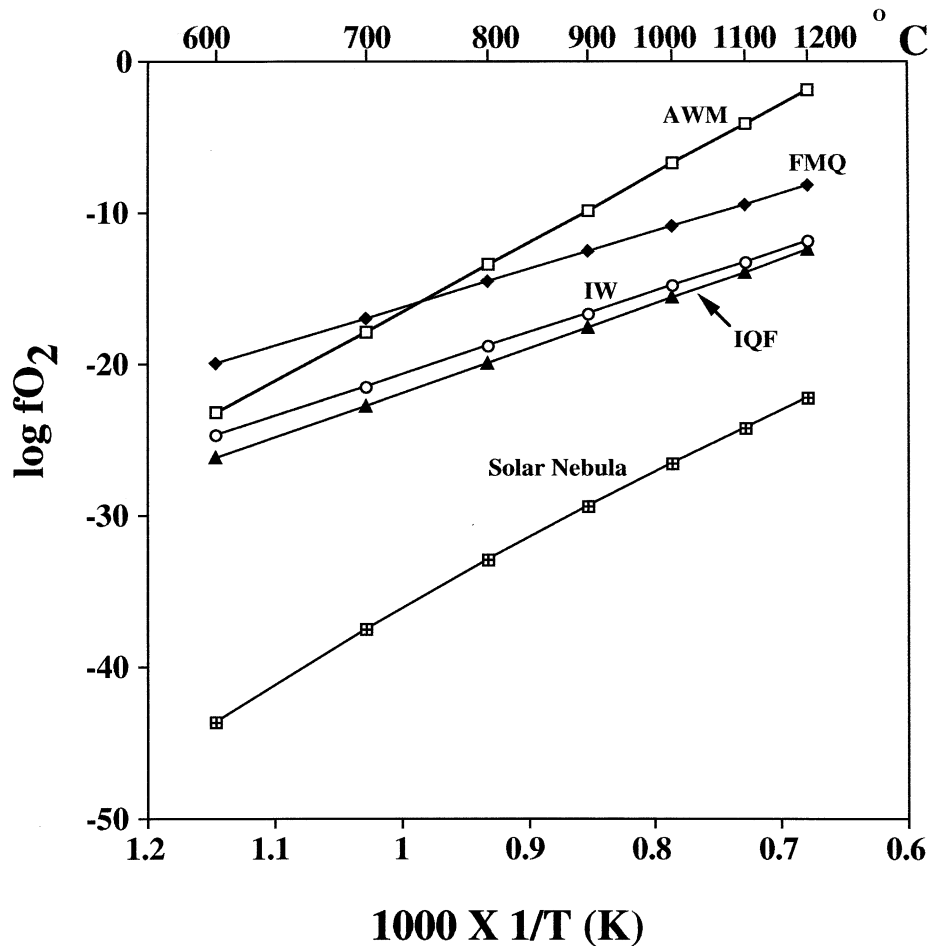
Fig. 26. Plots of log f_{O_2} vs. $1/T$ for the buffers andradite-wollastonite-magnetite (AWM), fayalite-magnetite-quartz (FMQ), iron-wüstite (IW), and iron-quartz-fayalite (IQF) are compared to the calculated f_{O_2} in the solar nebula.

interiors of the sinuous fragments but absent in the core of the host and in the rim sequence, the oxidation and alteration of these fragments must have taken place before incorporation of these objects. The presence of wollastonite + pure metallic Fe indicates reduction of both andradite and hedenbergite when this mineral was subjected to a lower f_{O_2} upon incorporation in the reduced CAI liquid. The reaction andradite to wollastonite + magnetite + O_2 was experimentally determined by Fehr (1992). Since the andradite-hedenbergite-wollastonite assemblages in Efremovka 101.1 contain no magnetite but pure Fe metal instead, magnetite must have been further reduced to metallic Fe. The reduction of andradite and hedenbergite must have taken place during incorporation of the sinuous fragments in the reduced refractory liquid of the host CAI. Figure 26 shows oxygen fugacity curves for various oxides in a log f_{O_2} vs. $1/T$ plot. Also shown in this figure is the solar nebular oxygen fugacity curve. This diagram indicates that the reduction of andradite to wollastonite + Fe requires a drop in f_{O_2} by 22 orders of magnitude at 1200°C. The petrographic settings of the sinuous fragments, the lack of alteration veins in melilite and rim sequence in the host, and the evidence for the reduction process leads to the conclusion that oxidation and alteration processes were active in the early solar system and perhaps

even predated melting of the CAI precursors and that f_{O_2} was quite variable in that region of the solar nebula where Efremovka 101.1 formed. Incorporation of the subinclusions took place when [26]Al was extant.

4.6. Formation of the Rim Layers

The change in the nature of mineral species in the successive rim layers from inside out is accompanied by a remarkable decrease in the abundances of the refractory oxides TiO_2, CaO, and Al_2O_3. It is also accompanied by a change in the Y/Zr ratio and a decrease in the total abundances of the REEs. However, we observe no change in the UR signature of the REE patterns from the innermost fassaite layer (layer 2) to the outermost olivine layer (layer 6).

The change in the diopside composition from layer 3 to layer 5 reflects the change in the chemistry of the source material that successively created these layers. The depletion in TiO_2 and the decrease in Al_2O_3 contents in layer 5 diopsides indicate a progressive depletion in these refractory oxides during the sequential deposition of the layers. This is important evidence against crystallization from a liquid that later enveloped the CAI. The systematic changes in rim layer compositions also

argue against their formation by evaporation, since such a process would inevitably lead to progressive enrichment in the refractory oxides in the outer layers. The abundances in REEs and RLTEs are systematically reduced by more than an order of magnitude from diopside D in layer 5 to olivine A in layer 6. The difference in the relative abundances of Y and Zr in fassaite (layer 2) and diopsides in layer 3 and 5 could not have resulted from crystal chemical effects, since these phases have the same crystal structure. These findings clearly indicate that (a) the rim layers did not form by crystal/liquid fractionation, (b) they did not crystallize from the host CAI, (c) they did not form by evaporation of the outer regions of the CAI, and (d) they originated from a source that was successively depleted in both REEs and RLEs along with a continuous decrease in the Y/Zr ratio as these layers were deposited onto the CAI, however without significant change in the UR REE signature of the individual mineral layers.

These constraints leave condensation as the only possible mechanism for the formation of the rim sequence. However, this conclusion is in conflict with equilibrium condensation calculations (Grossman, 1972; Lattimer et al., 1978). The equilibrium condensation model predicts that all the REEs and most of the RLTEs (e.g., Hf, Sc, Zr, and Y) must have condensed before diopside and olivine condense. It may appear plausible that the presence of the UR elements in all rim layers resulted from diffusion from fine-grained dust condensates highly enriched in REEs and RLTEs that might have coated every individual mineral grain before these grains accreted as individual successive layers. Diffusion of the refractory elements from the dust coatings into the individual grains could then have taken place either before accretion of the mineral layers or after accretion during a heating event. However, such a scenario requires the following prerequisites not supported by our findings: (a) If the diffusion took place before accretion then the different mineral species must have had distinct condensate coatings with distinct REE and RLE total abundances. Consequently, (1) the reservoir from which the rim layers condensed consisted of several subreservoirs, each characterized by a condensation of a distinct mineral species (Sc-fassaite, Al-diopside, diopside, Ca-rich olivine layer 4, and Ca-poor olivine layer 6); (2) each of these subreservoirs must have had fine-grained dust condensates with distinct UR compositions; and (3) mixing between these subreservoirs must have been inhibited; and (b) if the diffusion took place after all layers accreted, it is unclear why as a result all mineral layers did not display identical REE and RLTE total abundances. Such homogenization would have been easily promoted by grain boundary diffusion. We argue that this scenario cannot explain the mineralogical and trace element signatures of the individual layers. Consequently, the most plausible scenario is successive condensation of mineral species from a reservoir with a UR signature in which the abundances of UR elements are continuously decreasing.

4.7. Al-Mg Systematics

Although the Al-Mg system was disturbed in few sinuous fragments in a later impact event on the parent body, its study reveals important clues to the formation time of the CAI and the time of oxidation and alteration affecting the sinuous frag-

ments. Incorporation of subinclusions 1 and 2 into the host must have taken place very early, probably during partial melting. It is likely that both the sinuous fragments and the polygonal Cr-spinel-bearing refractory fragments were captured during the same event, since the subinclusions are attached to several sinuous fragments. The Cr-spinel-bearing refractory fragments are also crowded between the sinuous fragments. We hence maintain that their injection in the CAI melt along with the various families of perovskites, FeNi, and spinel clumps was contemporaneous with the sinuous fragments.

The oxidation and alteration of the rim sequence of subinclusion 1 and the sinuous fragments definitely occurred before their incorporation into the melt of the host CAI. The presence of the oxidized and later reduced andradite-hedenbergite-wollastonite-Fe-metal assemblage in the interiors of the sinuous fragments, with no conduits to the melilite grains in the core and the rim sequence of the inclusion supports our interpretation. The lack of any alteration in the melilite in the core also demonstrates that no alteration took place after melilite crystallization. This demonstrates that alteration and oxidation processes were active in the earliest stages of the solar system when ^{26}Al was still extant and that f_{O_2} was quite variable in the region of the solar nebula where Efremovka 101.1 was born. An evaporation mechanism through Rayleigh distillation for the formation of the CAI with its UR REE pattern can comfortably be ruled out, in view of the lack of equilibration between the various minerals and the presence of different ^{48}Ca/^{40}Ca ratios in three perovskites from different populations, and the absence of substantial Mg isotopic mass fractionation.

5. CONCLUSIONS

Efremovka 101.1 is a compact Type A CAI that experienced a very complex formation history that included accretion of precursor solids, partial melting, capture of solid early condensates, small CAIs and fragments of preexisting CAIs, solidification, and incorporation in the parent body followed by an impact event.

Our studies allow a reconstruction of the evolutionary processes experienced by the various components of the CAI. These stages are as follows:

1. All constituents of Efremovka 101.1 originated from the same region of the solar nebula, which is characterized by a UR REE pattern. This region had variable f_{O_2} conditions and Ca isotopic compositions. This region acted as a closed system with no material with a different REE signature contaminating its UR patterns. The UR pattern of the CAI did not result from evaporation of chondritic material but from condensation from a gas with this trace element chemical signature. Condensation of perovskite took place in various parts of this region from gases whose Y/Zr ratios were in part modified by removal of the most refractory ZrO$_2$ species. These subreservoirs also had different Ca isotopic compositions.
2. After accretion, 101.1 was subjected to a very short partial melting process. This was followed by incorporation of the different families of perovskite, FeNi metal, small CAIs,

and fragments of preexisting CAIs. Some of these CAIs had previously experienced alteration.

REFERENCES

Albee A. T. and Ray L. (1971) Correction factors for electron probe microanalysis of silicates, oxides, carbonates, phosphates, and sulfates. *Anal. Chem.* **42,** 1408–1414.

Anders A. and Grevesse N. (1989) Abundances of the elements: Meteoritic and solar. *Geochim. Cosmochim. Acta* **53,** 197–214.

Beckett J. R. (1986) *The Origin of Calcium-, Aluminium-Rich Inclusions From Carbonacious Chondrites: An Experimental Study.* Ph.D. thesis, University of Chicago.

Beckett J. R., Spivack A. J., Hutcheon I. D., Wasserburg G. J., and Stolper E. M. (1990) Crystal chemical effects on the partitioning of trace elements between mineral and melt: An experimental study of melilite with applications to refractory inclusions in carbonaceous chondrites. *Geochim. Cosmochim. Acta* **54,** 1755–1774.

Bence A. E. and Albee A. T. (1968) Empirical correction factors for the electron microanalysis of silicates and oxides. *J. Geol.* **76,** 382–403.

Boynton W. V. (1975) Fractionation in the solar nebula: Condensation of yttrium and the rare earth elements. *Geochim. Cosmochim. Acta* **39,** 569–584.

Boynton W. V., Frazier R. M., and Macdougall J. D. (1980) Identification of an ultra-refractory component in the Murchison meteorite. *Lunar Planet. Sci.* **11,** 103–105.

Colson R. O., McKay G. A., and Taylor L. A. (1989) Charge balancing of trivalent trace elements in olivine and low-Ca pyroxene: A test using experimental partitioning data. *Geochim. Cosmochim. Acta* **53,** 643–648.

Davis A. M. (1984) A scandalously refractory inclusion in Ornans. *Meteoritics* **19,** 214.

Davis A. M. (1991) Ultrarefractory inclusions and the nature of the Group II REE fractionation. *Meteoritics* **26,** 330.

Davis A. M. and Grossman L. (1979) Condensation and fractionation of rare earths in the solar nebula. *Geochim. Cosmochim. Acta* **43,** 1611–1632.

Davis A. M. and Hashimoto A. (1995) Volatility fractionation of rare earth elements and other trace elements during vacuum evaporation. *Meteoritics* **30,** 500–501.

Davis A. M., Hashimoto A., Clayton R. N., and Mayeda T. K. (1990) Isotope mass fractionation during evaporation of Mg_2SiO_4. *Nature* **347,** 655–658.

Davis A. M., Hashimoto A., Clayton R. N., and Mayeda T. K. (1995) Isotopic and chemical fractionation during evaporation of $CaTiO_3$. *Lunar Planet. Sci.* **26,** 317–318.

Dunn T. and McCallum F. S. (1982) The partitioning of Zr and Nb between diopside and melts in the system diopside-albite-anorthite. *Geochim. Cosmochim. Acta* **46,** 623–629.

El Goresy A., Palme H., Yabuki H., Nagel K., Herrwerth I., and Ramdohr P. (1984) A calcium-aluminum-rich inclusion from the Essebi (CM2) chondrite: Evidence for captured spinel-hibonite spherules and for an ultra-refractory rimming sequence. *Geochim. Cosmochim. Acta* **48,** 2283–2298.

El Goresy A., Zinner E. K., Matsunami S., Palme H., Spettel B., Lin Y., and Nazarov M. (1993) Efremovka 101.1: A primitive CAI with superrefractory REE patterns and enormous enrichments of Sc, Zr, and Y in fassaite and perovskite. *Meteoritics* **28,** 344–345.

Fahey A. J., Goswami J. N., McKeegan K. D., and Zinner E. (1987a)

^{26}Al, ^{244}Pu, ^{50}Ti, REE, and trace element abundances in hibonite grains from CM and CV meteorites. *Geochim. Cosmochim. Acta* **51,** 329–350.

Fahey A. J., Zinner E. K., Crozaz G., and Kornacki A. S. (1987b) Microdistributions of Mg isotopes and REE abundances in a Type A calcium-aluminum-rich inclusion from Efremovka. *Geochim. Cosmochim. Acta* **51,** 3215–3229.

Fehr T. (1992) *Petrogenetische Teil-Netze-für Niedertemperatur-Hochdruck (LT-HP)-Metamorphiten: System Ca-Al-Fe^{3+}-Ti-Si-O-H.* Habilitationsschr., Ludwig-Maximilian-Univ. München, Germany.

Floss C., El Goresy A., Zinner E., Kransel G., Rammensee W., and Palme H. (1996) Elemental and isotopic fractionations produced through evaporation of the Allende CV chondrite: Implications for the origin of HAL-type hibonite inclusions. *Geochim. Cosmochim. Acta* **60,** 1975–1997.

Floss C., El Goresy A., Zinner E., Palme H., Weckwerth G., and Rammensee W. (1998) Corundum-bearing residues produced through the evaporation of natural and synthetic hibonite. *Meteoritics Planet. Sci.* **33,** 191–206.

Gallahan W. E. and Nielsen R. L. (1992) The partitioning of Sc, Y, and the rare earth elements between high Ca-pyroxene and natural mafic to intermediate lavas at 1 atmosphere. *Geochim. Cosmochim. Acta* **56,** 2387–2404.

Goswami J. N., Srinivasan G., and Ulyanov A. A. (1991) Titanium, calcium and magnesium isotopic compositions in a hibonite-rich inclusion from Efremovka. *Meteoritics* **26,** 339.

Goswami J. N., Srinivasan G., and Ulyanov A. A. (1994) Ion microprobe studies of Efremovka CAIs: I. Magnesium isotope compositions. *Geochim. Cosmochim. Acta* **58,** 431–447.

Grossman L. (1972) Condensation in the primitive solar nebula. *Geochim. Cosmochim. Acta* **36,** 597–619.

Grossman L. (1975) Petrography and mineral chemistry of Ca-rich inclusions in the Allende meteorite. *Geochim. Cosmochim. Acta* **39,** 433–454.

Hinton R. W., Davis A. M., Scatena-Wachel D. E., Grossman L., and Draus R. J. (1988) A chemical and isotopic study of hibonite-rich refractory inclusions in primitive meteorites. *Geochim. Cosmochim. Acta* **52,** 2573–2598.

Ireland T. R. (1990) Presolar isotopic and chemical signatures in hibonite-bearing refractory inclusions from the Murchison carbonaceous chondrite. *Geochim. Cosmochim. Acta* **54,** 3219–3237.

Ireland T. R., Fahey A. J., and Zinner E. K. (1988) Trace-element abundances in hibonites from the Murchison carbonaceous chondrite: Constraints on high-temperature processes in the solar nebula. *Geochim. Cosmochim. Acta* **52,** 2841–2854.

Ireland T. R., Fahey A. J., and Zinner E. K. (1991) Hibonite-bearing microspherules: A new type of refractory inclusions with large isotopic anomalies. *Geochim. Cosmochim. Acta* **55,** 367–379.

Ireland T. R., Fahey A. J., Zinner E., and Esat T. M. (1992) Evidence for distillation in the formation of HAL and related hibonite inclusions. *Geochim. Cosmochim. Acta* **56,** 2503–2520.

Johnson M. L., Burnett D. S., and Woolum D. S. (1988) Relict refractory element rich phases in Type B CAI. *Meteoritics* **23,** 267.

Kennedy A. K., Hutcheon I. D., and Wasserburg G. J. (1991) Trace element distributions in compact type A CAI in Allende and Leoville. Evidence for relict perovskite. *Lunar Planet. Sci.* **22,** 709–710.

Kennedy A. K., Lofgren G. E., and Wasserburg G. J. (1994) Trace-element partition coefficient for perovskite and hibonite in meteorite compositions. *Chem. Geol.* **117,** 379–390.

Kennedy A. K., Beckett J. R., Edwards D.A., and Hutcheon I. D. (1997) Trace element equilibria and magnesium isotope heterogeneity in 3655A: Evidence for a complex multi-stage evolution of a typical Allende Type B1 CAI. *Geochim. Cosmochim. Acta* **61,** 1541–1561.

Kimura M., El Goresy A., Palme H., and Zinner E. (1993) Ca-, Al-rich inclusions in the unique chondrite ALH85085: Petrology, chemistry and isotopic compositions. *Geochim. Cosmochim. Acta* **57,** 2329–2359.

Kornacki A. S. and Fegley B. (1986) The abundance and relative volatility of refractory trace elements in Allende Ca, Al-rich inclusions: Implications for chemical and physical processes in the solar nebula. *Earth Planet. Sci. Lett.* **79,** 217–234.

Kruse H. (1979) Spectra processing with computer graphics. In *Conf. Computers in Activation Anal. and Gamma-Ray Spectrosc. Mayguez, Puerto Rico* **82,** 2228.

Lattimer J. M., Schramm D. N., and Grossman L. (1978) Condensation in supernova ejecta and isotopic anomalies in meteorites. *Astrophys. J.* **219,** 230–249.

Lindstrom D. J. (1976) *Experimental Study of the Partitioning of the Transition Metals Between Clinopyroxene and Coexisting Silicate Liquids.* Ph.D. thesis, University of Oregon.

Lundberg L. L., Zinner E., and Crozaz G. (1994) Search for isotopic anomalies in oldhamite (CaS) from unequilibrated (E3) enstatite chondrites. *Meteoritics* **29,** 384–393.

MacPherson G. J. and Davis A. M. (1993) A petrologic and ion microprobe study of a Vigarano Type B refractory inclusion: Evolution by multiple stages of alteration and melting. *Geochim. Cosmochim. Acta* **57,** 231–243.

MacPherson G. J., Grossman L., Allen J. M., and Beckett J. (1981) Origin of rims on coarse-grained inclusions in the Allende meteorite. In *Proc. Lunar Planet. Sci.* **12B,** 1079–1091. Pergamon, New York.

MacPherson G. J., Wark D. A., and Armstrong J. T. (1988) Primitive material surviving in chondrites: Refractory inclusions. In *Meteorites and the Early Solar System* (eds. J. F. Kerridge and M. S. Matthews), pp. 746–807. University of Arizona Press, Tucson.

Martin P. M. and Mason B. (1974) Major and trace elements in the Allende meteorite. *Nature* **249,** 333–334.

Mason B. and Martin P. M. (1977) Geochemical differences among components of the Allende meteorite. In *Mineral Sciences Investigations, Vol. 19* (ed. B. Mason), pp. 84–95.

McKeegan K. D., Walker R. M., and Zinner E. (1985) Ion microprobe isotopic measurements of individual interplanetary dust particles. *Geochim. Cosmochim. Acta* **49,** 1971–1987.

McSween H. Y., Jr. (1977) Petrographic variations among carbonaceous chondrites of the Vigarano type. *Geochim. Cosmochim. Acta* **41,** 1777–1790.

Palme H., Wlotzka F., Nagel K., and El Goresy A. (1982) An ultrarefractory inclusion from the Ornans carbonaceous chondrite. *Earth Planet. Sci. Lett.* **61,** 1–12.

Palme H., Hutcheon I. D., and Spettel B. (1994) Composition and origin of refractory-metal-rich assemblages in a Ca, Al-rich Allende inclusion. *Geochim. Cosmochim. Acta* **58,** 495–513.

Sheng Y. J., Hutcheon I. D., and Wasserburg G. J. (1991) Origin of plagioclase-olivine inclusions in carbonaceous chondrites. *Geochim. Cosmochim. Acta* **55,** 581–599.

Simon S. B., Grossman L., and Davis A. M. (1991) Fassaite composition trends during crystallization of Allende Type B refractory inclusion melts. *Geochim. Cosmochim. Acta* **55,** 2635–2655.

Simon S. B., Davis A. M., and Grossman L. (1992) Evidence for changes in redox state during crystallization of Allende Type B1 inclusions. *Meteoritics* **27,** 289–290.

Simon S. B., Kuehner S. M., Davis A. M., Grossman L., Johnson M. L., and Burnett D. S. (1994) Experimental studies of trace element partitioning in Ca-Al-rich compositions: Anorthite and perovskite. *Geochim. Cosmochim. Acta* **58,** 1507–1523.

Simon S. B., Davis A. M., and Grossman L. (1996) An ultrarefractory inclusion from the Murchison meteorite. *Meteoritics* **31,** 106–115.

Wang J., Davis A. M., and Clayton R. N. (1993) Rare earth element fractionation during evaporation of chondritic material. *Meteoritics* **28,** 454–455.

Wänke H., Kruse H., Palme H., and Spettel B. (1977) Instrumental neutron activation analysis of lunar samples and the identification of primary matter in the lunar highlands. *J. Radioanal. Chem.* **38,** 363–378.

Wark D. A. (1986) Evidence for successive episodes of condensation at high temperature in a part of the solar nebula. *Earth Planet. Sci. Lett.* **77,** 129–148.

Wark D. A. and Lovering J. F. (1977) Marker events in the early evolution of the solar system: Evidence from rims on Ca-Al-rich inclusions in carbonaceous chondrites. *Proc. Lunar Sci. Conf.* **8,** 95–112.

Weber D., Zinner E., and Bischoff A. (1995) Trace element abundances and Mg, Ca, and Ti isotopic compositions of grossite-containing inclusions from the carbonaceous chondrite Acfer 182. *Geochim. Cosmochim. Acta* **59,** 803–823.

Zinner E. and Crozaz G. (1985) A method for the quantitative measurement of rare earth elements in the ion microprobe. *Int. J. Mass Spectrometry Ion Processes* **69,** 17–38.

Zinner E. and El Goresy A. (1994) Evidence for extraneous perovskites in CAIs from the Efremovka (CV3) meteorite: A combined petrographic, trace element, and isotopic study. *Lunar Planet. Sci.* **25,** 1557–1558.

Appendix. Trace element concentrations in individual minerals.

Element	Mel A	Mel B	Mel C	Mel D	Mel E	Fas A	Fas B	Fas C	Fas D	Fas E	Fas F
K	29.2	74.6	11.3	3.58	67.1	119	103	19.9	49.4	35.0 ± 4.1	92.2
Sc	10.0	13.6	9.09	190	12.4	76,000	69,800	758	16,080	52,700	49,800
Ti	279	659	273	738	291	118,000	108,000	58,000	226,711	195,000	265,000
V	38.8	114	54.9	97.9	71.5	30,500	20,600	10,500	13,100	30,700	39,700
Cr	n.m.	n.m.	n.m.	n.m.	n.m.	n.m.	n.m.	n.m.	n.m.	n.m.	n.m.
Sr	232	216	224	236	230	215	270	54.5	190	226	167
Y	33.9	25.1	22.6	19.8	19.0	187	242	189	258	189	925
Zr	2.14	8.45	1.26 ± 0.14	19.3	3.71	10,320	15,100	1170	14,200	7790	26,600
Nb	0.02 ± 0.01	0.11 ± 0.02	0.01 ± 0.01	0.09 ± 0.02	0.01 ± 0.01	22.1 ± 2.4	22.8 ± 2.7	7.0	18.3	23.7 ± 2.4	75.8
Ba	22.5	32.5	30.6	26.1	27.9	27.2	28.6 ± 3.2	3.7 ± 0.4	22.0	16.6 ± 2.0	8.9 ± 1.4
Hf	n.m.	n.m.	n.m.	n.m.	n.m.	n.m.	n.m.	n.m.	n.m.	n.m.	n.m.
La	2.06	0.90 ± 0.10	1.07 ± 0.14	0.75	0.82	1.9 ± 0.2	3.2 ± 0.4	4.1	1.8 ± 0.2	1.6 ± 0.3	26 ± 3
Ce	4.1	1.88	2.45	1.76	1.54 ± 0.18	4.3	8.4 ± 1.2	15.2	5.2	6.8 ± 0.8	81.5
Pr	0.55 ± 0.07	0.33	0.31 ± 0.06	0.28	0.23 ± 0.03	1.0 ± 0.1	0.8 ± 0.2	2.0	1.2 ± 0.2	0.7 ± 0.3	13.7
Nd	2.95	1.46	1.67	1.28	1.37	4.1	5.4 ± 0.7	10.6	5.7	3.8 ± 0.6	66.7
Sm	1.06 ± 0.15	0.49 ± 0.07	0.56 ± 0.13	0.45 ± 0.06	0.44 ± 0.08	2.1 ± 0.3	0.8 ± 0.5	3.6 ± 0.4	2.6 ± 0.5	4.5 ± 0.8	19.0 ± 2.5
Eu	1.42	1.15	1.51	1.63	1.34	1.3	1.5 ± 0.3	0.3 ± 0.1	0.6 ± 0.2	1.0 ± 0.2	1.1 ± 0.3
Gd	3.03	2.58	1.57 ± 0.19	1.55	1.57 ± 0.18	8.0 ± 1.0	11.0 ± 1.4	11.4	8.9 ± 1.3	8.9 ± 1.1	64 ± 7
Tb	0.43 ± 0.07	0.37 ± 0.07	0.26 ± 0.06	0.24 ± 0.03	0.24 ± 0.04	1.5 ± 0.2	2.0 ± 0.4	2.4	2.3 ± 0.4	2.2 ± 0.3	10.5 ± 1.2
Dy	3.29	2.30	2.62	2.24	1.96	14.0	17.1	19.6	18.9	13.3	99.4
Ho	1.04	0.74 ± 0.09	0.64 ± 0.09	0.6 ± 0.07	0.56 ± 0.08	3.9 ± 0.5	5.5 ± 1.0	5.1	5.9 ± 0.6	4.4 ± 0.7	25.7
Er	3.05	2.17	1.84	1.7	1.71	15.0	20.7	18.9	25.0	20.4	83.5
Tm	0.11 ± 0.03	0.18 ± 0.02	0.08 ± 0.03	0.08 ± 0.03	0.07 ± 0.03	1.0 ± 0.1	1.6 ± 0.4	1.1	1.7 ± 0.2	1.4 ± 0.3	4.8 ± 0.6
Yb	0.53 ± 0.09	0.52 ± 0.07	0.61 ± 0.11	0.62	0.4 ± 0.08	6.5	7.8 ± 1.1	6.6	12.4 ± 1.4	8.0 ± 1.1	30.8
Lu	0.31 ± 0.06	0.29 ± 0.06	0.14 ± 0.04	0.2 ± 0.03	0.27 ± 0.04	8.1 ± 1.0	8.1 ± 1.1	4.2	14.8 ± 1.6	7.4 ± 1.2	12.5 ± 2.1

Element	Fas G	Fas H	Dio A	Dio B	Dio C	Rim Px D	O1A	O1B	Per-A	Per-B	Per-C
K	88.2	135	32.8	87.23	16.4	55.5	4.11	11.7	251	67.4 ± 3.5	46.6
Sc	73,000	62,800	58.7	45.04	648	80.6	4.8	2.5	5177	313	952
Ti	122,000	164,000	2411	1234	54,200	14,500	378	192	340,000	340,000	340,000
V	18,100	26,700	231	125	4290	1350	111	87	8740	2430	2990
Cr	501	321	n.m.	n.m.	n.m.	n.m.	n.m.	n.m.	409	407	418
Sr	270	254	53.3	31.7	54.3	38	4.05	1.54	n.m.	n.m.	n.m.
Y	226	234	28.6	53.4	268	88.1	2.8	0.59 ± 0.06	4040	2570	3020
Zr	11,900	7920	62.1	24.9	2000	220	4.6	1.45	16,700	5740	6970
Nb	21.7	23.1	1.29	1.15 ± 0.15	12.3	4.30 ± 0.49	0.071 ± 0.018	0.65	90.2	183	128
Ba	41.9	29.6	3.45	4.51	2.57 ± 0.32	1.69 ± 0.19	0.492 ± 0.085	1.58	27.4	17.7	16 ± 2
Hf	207	91.7 ± 14.3	n.m.	n.m.	n.m.	n.m.	n.m.	n.m.	n.m.	n.m.	n.m.
La	2.2 ± 0.3	2.4	0.44	0.60	4.1	1.85	0.078 ± 0.012	0.065 ± 0.009	163	75.1	88.3
Ce	7.5	6.2	1.29	1.94	14.7	5.58	0.311 ± 0.036	0.145 ± 0.015	378	212	229
Pr	1.1	1.0 ± 0.1	0.19	0.33 ± 0.03	2.12 ± 0.21	0.81	0.043 ± 0.009	0.019 ± 0.005	51.0	25.8	32 ± 4
Nd	5.6	5.6	0.99	1.52	10.7	3.93	0.130 ± 0.022	0.086 ± 0.014	288	157	202 ± 1
Sm	3.0 ± 0.4	2.2 ± 0.3	0.41	0.65 ± 0.10	3.56 ± 0.44	1.62 ± 0.18	0.052 ± 0.024	0.016 ± 0.014	83.1	62.0	71 ± 8
Eu	2.0	1.9	0.30	1.35	0.31 ± 0.07	0.24 ± 0.03	0.018 ± 0.006	0.015 ± 0.005	6.6 ± 0.7	5.0 ± 0.6	6.0 ± 0.9

(Continued)

Element	Fas G	Fas H	Dio A	Dio B	Dio C	Rim Px D	O1A	O1B	Per-A	Per-B	Per-C
Gd	8.2 ± 0.9	11.0	1.61	2.41	15.9	4.01	0.173 ± 0.030	0.039 ± 0.014	209	141	163 ± 16
Tb	2.3	2.0 ± 0.2	0.35	0.56 ± 0.07	3.42 ± 0.35	0.92 ± 0.09	0.036 ± 0.012	0.011 ± 0.004	52.9	32.3	34 ± 4
Dy	18.1	20.1	2.90	3.73	27.8	8.50	0.248 ± 0.030	0.057 ± 0.011	419	264	305
Ho	5.4	5.9	0.93	1.26 ± 0.14	7.4	3.01 ± 0.33	0.079 ± 0.017	0.020 ± 0.005	118	71.0	102
Er	24.4	26.2	2.99	5.68	25.3	8.65	0.230 ± 0.027	0.066 ± 0.011	378	227	272
Tm	1.6 ± 0.2	1.3 ± 0.2	0.16 ± 0.02	0.30 ± 0.06	1.24 ± 0.19	0.48	0.021 ± 0.007	0.008 ± 0.004	21.7	15.0	17 ± 2
Yb	10.5	11.8	1.51	2.12	9.80	4.12	0.129 ± 0.025	0.069 ± 0.014	88.9	57.2	92.9
Lu	8.8 ± 1.1	13.9 ± 1.4	0.80	1.00 ± 0.13	5.99 ± 0.68	1.90 ± 0.21	0.097 ± 0.018	0.033 ± 0.008	63.3	35.4	50.9

Element	Per-D	Per-E	Per-F	Per-G	Per-H	Per-I	Per-J	Per-K	Per-L	Per-M	Per-N
K	49.6	58.6	95.1	179	406.3	42.7	80.4	464.7	224.9	189.1	86.2
Sc	304	1336	531	766	850	204	1027	933	4170	516	678
Ti	340,000	340,000	340,000	340,000	340,000	340,000	340,000	340,000	340,000	340,000	340,000
V	4290	4830	2060	3500	4380	2690	5120	4170	12,000	25,600	2800
Cr	637	436	532	2490	1830	106	184	169	315	839	234
Sr	n.m.	n.m.	475	393	415	411	411	566	373	411	415
Y	5290	7210	4830	4620	2770	2070	8200	4620	4170	4040	5560
Zr	11,200	9120	5480	8700	9140	2200	6350	8040	8230	5240	7750
Nb	97.1	299	856	493	387	241	662	301	339	529	391
Ba	59.6	34	21.4	34 ± 4	56.6	24.2	32.5	61.3	21.9	23.1	55.5
Hf	n.m.	n.m.	47 ± 22	127 ± 27	71 ± 26	37 ± 9	49 ± 16	78 ± 17	107 ± 15	34 ± 11	412 ± 16
La	286	279	419	274	191	104	392	122	127	198	308
Ce	717	719	1199	784	551	278	1050	319	351	537	786
Pr	84.5	87.6	169	111	75.7	38.2	148	46.7	53.0	73.9	107
Nd	500	499	786	547	402	206	786	259	270	415	556
Sm	150	177	228	170	129	79.1	252	84.5	91.0	136	159
Eu	7.8 ± 0.9	5.8 ± 1.2	6.6 ± 1.0	7.1 ± 1.0	4.4 ± 0.9	5.6	7.8	8.1	5.3	5.6	5.6 ± 0.6
Gd	295	410	432	334	201	180	597	207	222	286	379
Tb	72.1	99.8	94.0	79.9	57.3	39.6	137	59.1	57.5	66.0	84.1
Dy	583	777	701	618	361	314	1075	483	437	514	696
Ho	150	251	185	159	98.3	81.2	302	148	133	136	189
Er	477	751	476	507	268	238	877	459	394	405	590
Tm	24.4	40.4	24.1	28.6	17.6	12.3	48.0	25.2	22.3	21.8	29.6
Yb	123	158	103	160	94.0	62.9	168	106	90.6	88.3	143
Lu	82.1	88.0	53.2	60.3	48.4	25.9	111	79.2	68.3	64.0	87.5

Concentrations are in ppm weight. 1σ errors due to countings statistics are given only if >10%.

n.m. = not measured.